



1 **A Deep-Learning Hybrid-Predictive-Modeling Approach for** 2 **Estimating Evapotranspiration and Ecosystem Respiration**

3 Jiancong Chen¹, Baptiste Dafflon², Anh Phuong Tran^{2,3}, Nicola Falco², and Susan S. Hubbard²

4 ¹Department of Civil and Environmental Engineering, University of California, Berkeley, CA, USA, ²Earth and
5 Environmental Sciences Area, Lawrence Berkeley National Laboratory, Berkeley, CA, USA, ³Department of Water
6 Resources Engineering and Technology, Water Resources Institute, 8, Phao Dai Lang, Dong Da, Hanoi, Vietnam

7
8 **Abstract:** Gradual changes in meteorological forcings (such as temperature and precipitation) are reshaping
9 vulnerable ecosystems, leading to uncertain effects on ecosystem dynamics, including water and carbon fluxes.
10 Estimating evapotranspiration (ET) and ecosystem respiration (R_{ECO}) is essential for analyzing the effect of climate
11 change on ecosystem behavior. To obtain a better understanding of these processes, we need to improve our estimation
12 of water and carbon fluxes over space and time, which is difficult within ecosystems where we have only sparse data.
13 In this study, we developed a hybrid predictive modeling approach (HPM) that integrates eddy covariance
14 measurements, physically-based model simulation results, meteorological forcings, and remote sensing datasets to
15 estimate evapotranspiration (ET) and ecosystem respiration (R_{ECO}) in high space-time resolution. HPM relies on a
16 deep learning algorithm-long short term memory (LSTM)-as well as direct measurements or outputs from physically-
17 based models. We tested and validated HPM estimation results at sites within various mountainous regions, given
18 their importance for water resources, their vulnerability to climate change, and the recognized difficulties in estimating
19 ET and R_{ECO} in mountainous regions. We benchmarked estimates of ET and R_{ECO} obtained from the HPM method
20 against measurements made at FLUXNET stations and outputs from the Community Land Model (CLM) at Rocky
21 Mountain SNOTEL stations. At the mountainous East River Watershed site in the Upper Colorado River Basin, we
22 explored how ET and R_{ECO} dynamics estimated from the new HPM approach vary with different vegetation and
23 meteorological forcings. The results of this study indicate that HPM is capable of identifying complicated interactions
24 among meteorological forcings, ET, and R_{ECO} variables, as well as providing reliable estimation of ET and R_{ECO}
25 across relevant spatiotemporal scales. With HPM estimation of ET and R_{ECO} at the East River Watershed, we found
26 that abiotic factors of temperature and radiation predominantly explained ET spatial variability; whereas R_{ECO}
27 variability was largely controlled by biotic factors, such as vegetation type. In general, our study demonstrated that
28 the HPM approach can circumvent the typical lack of spatiotemporally dense data needed to estimate ET and R_{ECO}
29 over space and time, as well as the parametric and structural uncertainty inherent in mechanistic models. While the
30 current limitations of the HPM approach are driven by the temporal and spatial resolution of available datasets (such
31 as NDVI), ongoing advances in remote sensing are expected to further improve accuracy and resolution of ET and
32 R_{ECO} estimation using HPM.

33 **1. Introduction:**

34 Evapotranspiration (ET) and ecosystem respiration (R_{ECO}) are key components of ecosystem water and
35 carbon cycles. ET is an important link between the water and energy cycles: dynamic changes in ET can affect
36 precipitation, soil moisture, and surface temperature, leading to uncertain feedbacks in the environment (Jung et al.,
37 2010; Seneviratne et al., 2006; Teuling et al., 2013). Thus, quantifying ET is particularly essential for improving our



38 understanding of water and energy interactions and watershed response to abrupt and gradual changes in climate,
39 which is critical for water resources management, agriculture, and other societal benefits (Anderson et al., 2012; Jung
40 et al., 2010; Rungee et al., 2019; Viviroli et al., 2007; Viviroli and Weingartner, 2008). R_{ECO} describes the sum of
41 autotrophic respiration and respiration by heterotrophic microorganisms in a specific ecosystem and plays a vital role
42 in the response of terrestrial ecosystem to global change (Jung et al., 2017; Reichstein et al., 2005; Xu et al., 2004).
43 As long term exchanges in R_{ECO} have pivotal influences over the climate system (Cox et al., 2000; Gao et al., 2017;
44 IPCC, 2019; Suleau et al., 2011), approaches are needed to estimate and monitor R_{ECO} over relevant spatiotemporal
45 scales. As described below, there are many different strategies for measuring and estimating ET and R_{ECO} , each of
46 which has advantages and limitations. The motivation for this study is the recognition that current methods cannot
47 provide ET and R_{ECO} at space and time scales needed to improve prediction of changing terrestrial system behavior,
48 particularly in challenging mountainous watersheds.

49 Several ground-based approaches have been used to provide *in situ* estimates or measurements of ET and
50 R_{ECO} . Ground based flux chambers capture and measure trace gases emitted from the land surface, which can be used
51 to estimate ET and R_{ECO} (Livingston and Hutchinson, 1995; Pumpanen et al., 2004). However, the microclimate of
52 the environment is affected by the chamber, and the laborious acquisition process and small chamber size typically
53 lead to information with coarse spatiotemporal resolution (Baldocchi, 2014). The eddy covariance method uses a tower
54 with installed instruments to autonomously measure fluxes of trace gases between ecosystem and atmosphere
55 (Baldocchi, 2014; Wilson et al., 2001). The covariance between the vertical velocity and mixing ratios of the target
56 scalar is computed to obtain the fluxes of carbon, water vapor, and other trace gases emitted from the land surface. ET
57 is then calculated from the latent heat flux, and R_{ECO} is calculated from the net carbon fluxes using night-time or
58 daytime partitioning approaches (van Gorsel et al., 2009; Lasslop et al., 2010; Reichstein et al., 2005). The spatial
59 footprint of obtained fluxes is on the order of hundreds of meters, and the temporal resolution of the measurements
60 range from hours to decades (Wilson et al., 2001). Such *in situ* measurements of fluxes have been integrated into the
61 global network of AmeriFlux (<http://ameriflux.lbl.gov/>) and FLUXNET (<https://FLUXNET.fluxdata.org/>), where
62 such data have strongly supported scientists in process understanding and model development. Given the cost, efforts,
63 and power required to install and maintain a flux tower, eddy covariance towers are typically sparse relative to the
64 scale of study sites used to address ecosystem questions. Additionally, the location of a flux tower within a watershed
65 greatly influences measurement representativeness. For example, eddy covariance towers are usually installed at
66 valley bottoms of mountainous watersheds (Strachan et al., 2016), and estimates obtained there may not be
67 representative of fluxes across a range of elevations or slope aspects within the watershed. The limited number of
68 towers and their limited ability to sample different portions of a watershed thus limit the usefulness of flux towers for
69 estimating ET and R_{ECO} in high resolution over space and time.

70 Physically-based models, which numerically represent land-surface energy and water balance, have also been
71 used to estimate ET and R_{ECO} (Tran et al., 2019; Williams et al., 2009). These physically-based models solve physical
72 equations to simulate the exchanges of energy, heat, water and carbon across atmosphere-canopy-soil compartments.
73 Examples include the Community Land Model (CLM, Oleson et al., 2013). Performance of these models depend on



74 the accuracy of inputs and parameters, such as soil type and leaf area index, which can be difficult to obtain at
75 sufficiently high spatiotemporal resolution. The lack of measurements to infer parameters needed for models often
76 leads to large discrepancies between model-based and flux-tower-based ET and R_{ECO} estimates. Conceptual model
77 uncertainty inherent in mechanistic models can also lead to ET and R_{ECO} estimation uncertainty and errors. For
78 example, Keenan et al. (2019) suggested that current terrestrial carbon cycle models neglect inhibition of leaf
79 respiration that occurs during daytime, which can result in a bias of up to 25%. These conceptual uncertainties, in
80 addition to data sparseness and data uncertainty, further limit the applicability of physically-based models to estimate
81 ET and R_{ECO} at high spatiotemporal scales. Semi-analytical formulations based on combinations of meteorological
82 and empirical parameters provide a reference condition for the water and energy balance. Examples used to estimate
83 potential ET include the Budyko framework and its extensions (Budyko, 1961; Greve et al., 2015; Zhang et al., 2008);
84 the Penman-Monteith's equation (Allen et al., 1998), and the Priestley-Taylor equation (Priestley and Taylor, 1972).
85 Actual ET can then be approximated by multiplying a coefficient associated with water deficit (De Bruin, 1983;
86 Williams & Albertson, 2004). However, even with these empirical formulations many attributes are still difficult to
87 obtain globally at high temporal scales, such as water-vapor deficit, leaf area index, and aerodynamic conductance of
88 different plants.

89 Remote sensing products, such as Landsat imagery (Irons et al., 2012) and the moderate-resolution imaging
90 spectroradiometer (MODIS, NASA, 2008), have also been integrated to estimate ET and R_{ECO} with empirical,
91 statistical, or semi-physical relations (Abatzoglou et al., 2014; Dagggers et al., 2018; Mohanty et al., 2017; Paca et al.,
92 2019). Due to the high spatial coverage of remote sensing products, global-scale estimates of ET and R_{ECO} have
93 become feasible. For example, Ryu et al. (2011) proposed the Breathing Earth System Simulator approach, which
94 integrates mechanistic models and MODIS data to quantify ET and GPP with a spatial resolution of 1-5 km and a
95 temporal resolution of 8 days. Ai et al. (2018) extracted enhanced vegetation index, fraction of absorbed
96 photosynthetically active radiation, and leaf area index from the MODIS dataset—and used the rate-temperature curve
97 and strong correlations between terrestrial carbon exchange and temperature to estimate R_{ECO} at 1 km spatial
98 resolution and 8-day temporal resolution. Ma et al. (2018) developed a data fusion scheme that fused Landsat-like-
99 scale datasets and MODIS data to estimate ET and irrigation water efficiency at a spatial scale of ~100 meters.
100 However, even though remote sensing data cover large areas of the earth surface, they typically do not provide
101 information over both high spatial and temporal resolution, and are also subject to cloudy conditions. For example,
102 Landsat has average return periods of 16 days with a spatial resolution of 30 m (visible and near-infrared), whereas
103 MODIS has 1-2 days temporal resolution with a 250 m or 1 km spatial resolution depending on the sensors. These
104 resolutions are typically too coarse to enable exploration of how aspects such as plant phenology, snowmelt, and
105 rainfall impact integrated ecosystem water and energy dynamics.

106 Combining machine-learning models with remote sensing products and meteorological inputs offers another
107 option for large-scale estimation of ET and R_{ECO} . Remotely sensed data are good proxies for plant productivity and
108 can be easily implemented into machine-learning models for ET and R_{ECO} estimation, such as for an enhanced
109 vegetation index, land surface water index and NDVI (Gao et al., 2015; Jägermeyr et al., 2014; Migliavacca et al.,



110 2015). Li and Xiao (2019) developed a data-driven model for gross primary production at a spatial and temporal
111 resolution of 0.05° and 8 days using MODIS and meteorological reanalysis data. Berryman et al. (2018) demonstrated
112 a Random Forest model to predict growing season soil respiration from subalpine forests in the Southern Rocky
113 Mountains ecoregion. Jung et al. (2009) developed a model tree ensemble approach to upscale FLUXNET data, where
114 they have successfully estimated ET and GPP. Other methods have used support vector machines, artificial neural
115 networks, random forest, and piecewise regression (Bodesheim et al., 2018; Metzger et al., 2013; Xiao et al., 2014;
116 Xu et al., 2018). These models were trained with ground-measured flux observations and other variables, and then
117 applied to estimate ET over continental or global scales with remote sensing and meteorological inputs. Some of the
118 most important inputs include the enhanced vegetation index, aridity index, temperature, and precipitation. However,
119 the spatiotemporal resolution of these approaches is constrained by the resolution of remote sensing products and
120 meteorological inputs. Additionally, parameters such as leaf area index, cloudiness, and the vegetation types required
121 by those models may not be available at the required resolution, accuracy or location. For example, in systems that
122 have significant elevation gradients, errors may result when valley-based FLUXNET data are used for training and
123 then applied to hillslope or ridge ET and R_{ECO} estimation

124 Development of hybrid models that link direct measurements and/or interpretable mechanistic models with
125 data-driven methods can benefit ET and R_{ECO} estimation (Reichstein et al., 2019). While remote sensing data that
126 cover large regions provide promise for informing models, quantitative interpretation of these data needed for input
127 into mechanistic models is still challenging (Reichstein et al., 2019). Physically-based models can provide estimates
128 of ET and R_{ECO} , but the estimate error can be high, owing to parametric, structural, and conceptual uncertainties as
129 described above. Hybrid data-driven frameworks are potentially advantageous because they enable the integration of
130 remote sensing datasets, meteorological forcings, and mechanistic model outputs of ET and R_{ECO} into one model.
131 Machine-learning approaches are then applied to extract the spatiotemporal patterns for ET and R_{ECO} prediction.
132 Hybrid models can utilize the high spatial coverage of remote sensing data (e.g., 30 m of Landsat) and high temporal
133 resolution of direct measurement from flux towers or simulation results from mechanistic models (e.g., daily or hourly
134 scales), thus providing alternative approaches for next-stage, more accurate estimation of ET and R_{ECO} at greater
135 spatial and finer temporal scales—and enhancing our process understanding of water and carbon cycling under climate
136 change.

137 In this study, we developed a hybrid predictive modeling approach (HPM) to better estimate ET and R_{ECO}
138 over space and time with easily acquired meteorological data (i.e., air temperature, precipitation and radiation) and
139 remote sensing products (i.e., NDVI). HPM is hybrid as it can use deep learning models to integrate direct
140 measurements from flux towers and physically-based model results (e.g., CLM) with meteorological and remote
141 sensing inputs to capture the complex physical interactions within the watershed ecosystem. After development, we
142 validated HPM performance with the FLUXNET dataset and benchmarked the CLM model at select sites. We then
143 used the HPM for ET and R_{ECO} estimation at the mountainous East River Watershed in CO and investigated how
144 small-scale heterogeneity influences ET and R_{ECO} dynamics.



145 The remainder of this paper is organized as follows. Section 2 mainly describes the sites considered in this
146 study and how data were acquired and processed. Section 3 presents the methodology of the HPM approach, followed
147 by the results of various use cases presented in Section 4. Discussion and conclusion are provided in Sections 5 and
148 6, respectively.

149 **2. Site Information, Data Acquisition and Processing**

150 We selected various sites to develop and validate our approaches. We focused on mountainous watersheds
151 because they provide significant water resources to the world (Viviroli et al., 2007), but also included sites to test
152 HPM's capabilities under different climate and vegetation conditions. Mountainous watersheds are very sensitive to
153 changes in temperature and precipitation patterns, which can significantly threaten downgradient water resources and
154 associated societal benefits (Breshears et al., 2005; Ernakovich et al., 2014; Immerzeel et al., 2019). As mountainous
155 regions are extremely important for regional and global assessment and management of water resources and carbon
156 storage and emission (Knowles et al., 2015; Schimel et al., 2002), accurate estimation of ET and R_{ECO} in these regions
157 is critical, though challenging due to complex heterogeneity and complicated interactions among the hydrosphere,
158 biosphere and the atmosphere (Pelletier et al., 2018; Speckman et al., 2015). Thus, we focused on estimating ET and
159 R_{ECO} at various sites along the Rocky Mountains, including the East River Watershed (Hubbard et al., 2018) of the
160 Upper Colorado River Basin.

161 **2.1 FLUXNET Stations and Ecoregions**

162 Eight FLUXNET stations were selected for this study (Table 1 and Figure 1), which cover a wide range of
163 climate and vegetation types. These stations have elevations from 129 m (US-Var) to 3050 m (US-NR1), mean annual
164 air temperature from 1.5°C (US-NR1) to 17.92°C (US-SRM), and mean annual precipitation from 320 mm (US-Whs)
165 to 800 mm (US-NR1). These FLUXNET stations also cover a wide range of vegetation types (i.e., evergreen forest,
166 deciduous forest, and shrublands). As indicated by Hargrove et al. (2003), FLUXNET stations provide a good
167 representation of different ecoregions, which are areas that display recurring patterns of similar combinations of soil
168 and landform characteristics (Omernik, 2004). Omernik & Griffith. (2014) delineated the boundaries of ecoregions
169 through pattern analysis that consider the spatial correlation of both physical and biological factors (i.e., soils,
170 physiography, vegetation, land use, geology and hydrology) in a hierarchical level. FLUXNET stations considered in
171 this study mainly locate in 4 unique ecoregions (Table 1). As is described below, we developed local-scale (i.e., point
172 scale) HPM that are representative for different ecoregions using data provided at these FLUXNET stations to estimate
173 ET and R_{ECO} , and validated the HPM estimates with measurements from stations within the same ecoregion.

174 **2.2 SNOTEL Stations**

175 For reasons described below, we performed a deeper exploration within one of the mountainous watershed
176 sites (the East River Watershed of the Upper Colorado River Basin), which is located in the “western cordillera”
177 ecoregion. At this site, we utilized meteorological forcings data from three snow telemetry (SNOTEL) stations. These
178 sites include the Butte (ER-BT, id: 380), Porphyry Creek (ER-PK, id: 701) and Schofield Pass (ER-SP, id: 737) sites.
179 A CLM model was developed at these SNOTEL stations that provides physically-model-based ET estimation (Tran

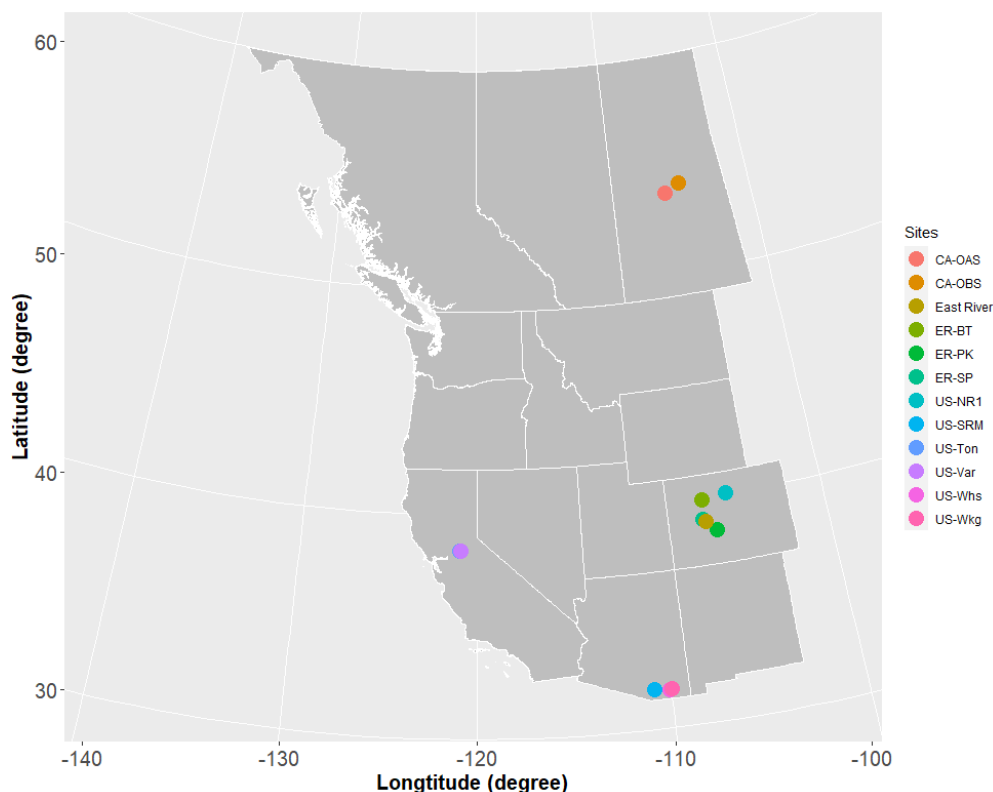


180 et al., 2019). Table 1 summarizes the SNOTEL stations used in this study and the corresponding climate characteristics.
 181 Figure 1 shows the geographical locations of FLUXNET and SNOTEL stations selected in this study.

182 **Table 1. Summary of FLUXNET stations and SNOTEL stations information. * denotes SNOTEL stations and all others**
 183 **are FLUXNET stations. Dfc, Bsk, Csa represent subarctic or boreal climates, semi-arid climate, Mediterranean hot summer**
 184 **climates, respectively. ENF, DBF, WSA, GRA, and OSH represent evergreen needleleaf forest, deciduous broadleaf forests,**
 185 **woody savannas, grasslands, open shrubland, respectively.**

| Site ID | Site Name | Latitude, Longitude | Elevation (m) | Mean Annual temperature (°C) | Mean Annual Precipitation (m) | Climate Koepfen | Vegetation IGBP | Ecoregions (Level II) | Period of Record |
|---------|---------------------------------|----------------------|---------------|------------------------------|-------------------------------|-----------------|-----------------|-------------------------------|------------------|
| US-NR1 | Niwot Ridge | (40.0329, -105.5464) | 3050 | 1.5 | 800 | Dfc | ENF | Western Cordillera | 2000-2014 |
| CA-Oas | Saskatchewan-Aspen | (53.6289, -106.1978) | 530 | 0.34 | 428.53 | Dfc | DBF | Boreal Plain | 1997-2010 |
| CA-Obs | Saskatchewan-Black Spruce | (53.9872, -105.1178) | 628.94 | 0.79 | 405.6 | Dfc | ENF | Boreal Plain | 1999-2010 |
| US-SRM | Santa Rita Mesquite | (31.8214, -110.8661) | 1120 | 17.92 | 380 | Bsk | WSA | Western Sierra Madre Piedmont | 2005-2015 |
| US-Ton | Tonzi Ranch | (38.4316, -120.9660) | 177 | 15.8 | 559 | Csa | WSA | Mediterranean California | 2002-2015 |
| US-Var | Vaira Ranch-lone | (38.4133, -120.9507) | 129 | 15.8 | 559 | Csa | GRA | Mediterranean California | 2002-2015 |
| US-Whs | Walnut Gulch Lucky Hills Shrub | (31.7438, -110.0522) | 1370 | 17.6 | 320 | Bsk | OSH | Western Sierra Madre Piedmont | 2008-2015 |
| US-Wkg | Walnut Gulch Kendall Grasslands | (31.7365, -109.9419) | 1531 | 15.64 | 407 | Bsk | GRA | Western Sierra Madre Piedmont | 2005-2015 |
| ER-BT* | East River-Butte | (38.894, -106.945) | 3096 | 2.38 | 821 | Dfc | N/A | Western Cordillera | 1995-2017 |
| ER-SP* | East River-Schofield Pass | (39.02, -107.05) | 3261 | 2.46 | 1064 | Dfc | N/A | Western Cordillera | 1995-2017 |
| ER-PK* | East River-Porphry Creek | (38.49, -106.34) | 3280 | 1.97 | 574 | Dfc | N/A | Western Cordillera | 1995-2017 |

186



187

188 **Figure 1. Location of sites considered in this study. Note: US-Ton and US-Var; US-Whs and US-Wkg are at the**
189 **locations. East River Watershed is located next to ER-BT. The white lines delineate Western US states and Canadian**
190 **provinces.**

191 2.3 East River Watershed and Previous Analyses

192 Data from the East River Watershed were used to explore how ET and R_{ECO} dynamics estimated from the
193 developed HPM vary with different vegetation and meteorological forcings. The East River Watershed is located
194 northeast of the town of Crested Butte, Colorado. This watershed has an average elevation of 3266 m, with significant
195 gradients in topography, hydrology, geomorphology, vegetation, and weather. The watershed has a mean annual
196 temperature around 0°C, with an average of 1200 mm yr⁻¹ total precipitation (Hubbard et al., 2018). Consisting of
197 montane, subalpine, and alpine life zones, each with distinctive vegetation biodiversity, the East River Watershed is a
198 testbed for the US Department of Energy Watershed Function Scientific Focus Area Project, led by the Lawrence
199 Berkeley National Laboratory (LBNL; Hubbard et al., 2018). The project has acquired a range of datasets, including
200 hydrological, biogeochemical, remote sensing, and geophysical datasets.

201 Recently completed studies at the East River Watershed were used in this study to inform HPM and to assess
202 the results. For example, physically-model-based estimations of ET at this site (Tran et al., 2019) were used herein for
203 HPM development and validation. Falco et al. (2019) used machine-learning-based remote sensing methods to

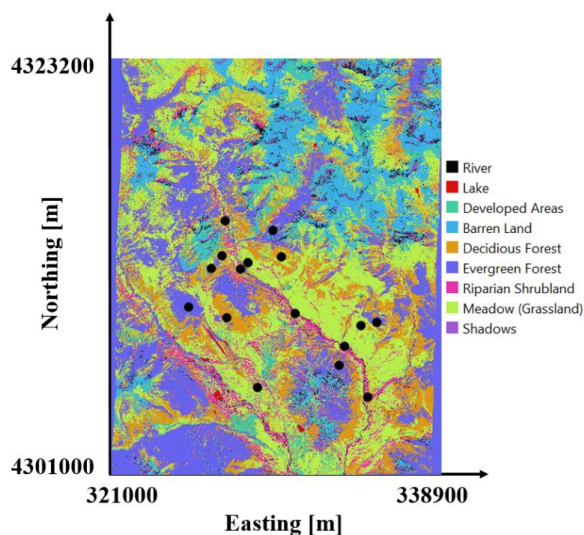


204 characterize the spatial distribution of vegetation types, slopes, and aspects within a hillslope at the East River
 205 Watershed, which were used with obtained HPM estimates to explore how small-scale vegetation heterogeneity
 206 influences ET and R_{ECO} dynamics. To perform this assessment, we computed the spatial distribution of vegetation
 207 types at watershed scale, based on Falco et al. (2019), and selected 16 locations within the East River Watershed
 208 having different vegetation types and slope aspects. These 16 locations were chosen at a level to be distinguishable
 209 by Landsat images and maintain the same vegetation type (given a spatial resolution of 30 m), and also possess small-
 210 scale heterogeneity. A summary of the locations is presented in Table 2; the spatial distribution of the locations is
 211 shown in Figure 2.

212 **Table 2: Location and vegetation types of East River Watershed sampling points (Figure 2)**

| Easting (m) | Northing (m) | Vegetation Type | Aspect | Elevation (m) |
|-------------|--------------|--------------------|--------|---------------|
| 327085 | 4309878 | Deciduous Forest | South | 2983 |
| 326288 | 4312504 | Deciduous Forest | South | 3177 |
| 330012 | 4313132 | Deciduous Forest | North | 3108 |
| 326854 | 4313192 | Deciduous Forest | South | 3098 |
| 328246 | 4312832 | Meadow | South | 3095 |
| 327010 | 4315059 | Meadow | South | 2790 |
| 328738 | 4306139 | Meadow | North | 2890 |
| 334270 | 4309465 | Meadow | North | 2929 |
| 333406.5 | 4308340 | Riparian Shrubland | South | 2760 |
| 327846 | 4312497 | Riparian Shrubland | South | 2723 |
| 334641 | 4305632 | Riparian Shrubland | North | 2740 |
| 330760 | 4310097 | Riparian Shrubland | South | 2855 |
| 329573 | 4314569 | Evergreen Forest | South | 3026 |
| 333106 | 4307313 | Evergreen Forest | North | 3102 |
| 325056 | 4310456 | Evergreen Forest | South | 2961 |
| 335141 | 4309614 | Evergreen Forest | North | 3131 |

213



214

215 **Figure 2: Vegetation classification of the East River, CO Watershed from Falco et al. (2019). East River sites selected in**
 216 **this study are denoted by black circles.**

217 **2.4 Data Collection and Processing**



218 To enhance transferability of the developed HPM strategy to less intensively characterized watersheds, we
219 selected only “easy to measure” or “widely available” attributes, such as precipitation, temperature, radiation and
220 NDVI, as inputs to the HTM model. The data sources used for these inputs include FLUXNET data
221 (<https://fluxnet.fluxdata.org/>), SNOTEL data (<https://www.wcc.nrcs.usda.gov/snow/>) and developed CLM model
222 (Tran et al., 2019) at SNOTEL stations, DAYMET meteorological inputs (Thornton et al., 2017) and remote sensing
223 data from Landsat imageries (Irons et al., 2012).

224 A variety of measured data and model outputs were used to train and validate HPM. We obtained daily
225 meteorological data, including air temperature, precipitation, radiation, ET, and R_{ECO} data, from the FLUXNET
226 database at the selected FLUXNET sites. The pipeline of data processing for FLUXNET dataset is provided at
227 <https://FLUXNET.fluxdata.org/>. ET data for US-NR1 were cleaned following the procedures presented in Rungee et
228 al. (2019). The meteorological data were used as inputs for HPM development, and ET and R_{ECO} data from these sites
229 were used for HPM validation. At the three selected SNOTEL stations, we obtained air temperature, precipitation, and
230 snow-water-equivalent data from the SNOTEL database. Air temperature data at these three SNOTEL stations were
231 processed following Oyler et al. (2015), given potential systematic artifacts. Snow-water-equivalent data are not easily
232 acquired, and thus were not considered as inputs for HPM. However, a categorical variable was constructed to
233 assimilate information regarding snow (Section 3.2.1). CLM models were generated following Tran et al. (2019) for
234 the SNOTEL stations and US-NR1 to assess the spatiotemporal variability of ET at the East River Watershed and for
235 training and validating HPM (Section 4.3). The DAYMET dataset (Thornton et al., 2017) provided gridded daily
236 weather-forcings-attribute estimates at a 1 km spatial resolution. We obtained the incident radiation data from
237 DAYMET at the SNOTEL stations as inputs for HPM. For the East River Watershed sites, meteorological forcings
238 data, including air temperature, precipitation and radiation, were also obtained from DAYMET. The low spatial
239 resolution of DAYMET data introduces uncertainty in HPM estimation of ET and R_{ECO} , which will be discussed in
240 the following sections. We calculated the NDVI time series from the red band (RED) and near-infrared band (NIR)
241 from Landsat 5, 7, and 8 images following Equation 1 at all selected FLUXNET sites, SNOTEL stations, and East
242 River Watershed sites at a spatial scale of 30 m.

$$243 \quad NDVI = \frac{NIR - RED}{NIR + RED} \quad (1)$$

244 Since cloud conditions can severely decrease data quality, we used the cloud-scoring algorithm provided in the Google
245 Earth Engine to mask clouds in all retrieved data, only selecting the ones that had a simple cloud score below 20 to
246 ensure data quality. Given the different calibration sensors used in Landsat 5, 7, and 8, we also followed the processes
247 described in Homer et al. (2015) and Vogelmann et al. (2001) to keep NDVI computations consistent over time.
248 Landsat satellites have a return period of 16 days, and thus we performed a reconstruction of NDVI time series to
249 obtain daily scale time data (Section 3.2.2).

250 3. Hybrid Predictive Modeling Framework

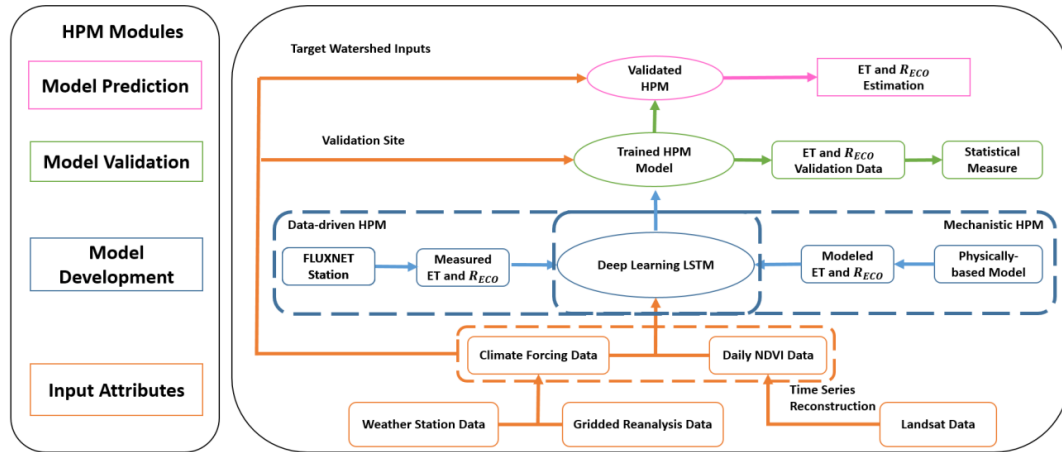


251 In this section, we illustrate the steps for building an HPM model for ET and R_{ECO} estimation over time and
252 space. Figure 3 presents the general framework of HPM, which includes modules for data preprocessing, model
253 development, model validation, and predictive modeling.

254 3.1 Model Framework

255 HPM establishes relationships among meteorological forcings attributes, NDVI, ET, and R_{ECO} (Figure 3).
256 Both input data (e.g., meteorological forcings) and output data (ET and R_{ECO}) used for training and validation are
257 preprocessed for gap filling, smoothing, and data updating. HPM “learns” the complex space-time relationship among
258 meteorological forcings, NDVI, ET, and R_{ECO} using a deep-learning-based module (deeply connected neural networks
259 and a long short-term memory recurrent neural network). HPM then can be used for ET and R_{ECO} estimation at
260 sparsely monitored watersheds. Individual HPM models can be trained in two different ways using ET and R_{ECO}
261 information: with data obtained from flux towers (“data-driven HPM”) or with outputs from 1-D physically-based
262 models (“mechanistic HPM”). In both cases, the models obtained with local data are then used to estimate ET and
263 R_{ECO} at other sites in the same ecoregion (see Section 2.1). For ecoregions not represented by FLUXNET sites, it is
264 necessary to develop mechanistic HPM that enables ET and R_{ECO} estimation over space and time.

265 HPM has several additional modules, including model development, model validation, and model prediction
266 modules. In the HPM model development module, deep-learning algorithms are trained with input features and
267 response data until a pre-defined “stopping criteria” (e.g., root mean squared error, RMSE) is met, indicating
268 subsequent training would lead to minimal improvement. In the validation module, estimation outputs from the
269 “trained HPM models” are compared with other ET and R_{ECO} data obtained from other independent sites or
270 mechanistic models within the same ecoregion. Statistical measures, including adjusted R^2 and mean absolute error
271 (MAE), are computed to evaluate the performance of HPM models. In the predictive model module, meteorological
272 forcings data and remote sensing data are processed at target sites of interest, and the validated HPM model is used to
273 estimate ET and R_{ECO} at these sites. ET and R_{ECO} outputs estimated from HPM at sparsely monitored watersheds then
274 provide alternative datasets for process understanding within the target watersheds.



275

276 **Figure 3: Hybrid Predictive Model Framework.** The HPM model mainly consists of four modules: **Input Attributes**, **Model**
 277 **Development**, **Model Validation** and **Model Prediction**, represented by rectangles with colors. Arrows represent the linkages
 278 among different modules. Choices of data-driven HPM or mechanistic HPM depend on the ecoregion of target watershed
 279 and data availability.

280 Long short-term memory (LSTM, Hochreiter & Schmidhuber, 1997) is capable of identifying long-term
 281 dependencies between climate and environmental data. For example, Kratzert et al. (2018) successfully used LSTM
 282 to learn the long-term dependencies in hydrological data (e.g., storage effects within catchments, time lags between
 283 precipitation inputs and runoff generation) for rainfall-runoff modeling. LSTM has also been used for gap filling in
 284 hydrological monitoring networks in the spatiotemporal domain (Ren et al., 2019). In this study, the outputs (ET or
 285 R_{ECO}) denoted as y are predicted from the input $x = [x_1, x_2, \dots, x_T]$, consisting of the last T consecutive time steps of
 286 attributes, such as meteorological forcings attributes (e.g., air temperature and precipitation) and remote sensing
 287 attributes (i.e., NDVI). In a recurrent neural network (RNN), h_t represents the internal state at every time step t that
 288 takes in current input value x_t and previous internal state h_{t-1} , and is recomputed along the time axis using the
 289 following equation:

$$290 \quad h_t = g(Wx_t + Uh_{t-1} + b), \quad (2)$$

291 where g represents the hyperbolic tangent activation function, W and U are trainable weight metrics of the hidden
 292 state h , and b is a bias vector. W , U and b are all trainable through optimization. LSTM introduces the cell state c_t ,
 293 which makes LSTM powerful in identifying long-term dependencies in a statistical manner. The cell state c_t has three
 294 gates structures, including “forget gates” (which determine what information from previous cell states will be
 295 forgotten), “input gates” (which determine what information will be conveyed from the forget gate) and “output gates”
 296 (which return information from cell state c_t to a new state h_t). With these gate structures, the cell state c_t controls
 297 what information will be forgotten, conveyed, and updated over time. The forget gate is formulated as follows:

$$298 \quad f_t = \sigma(W_f x_t + U_f h_{t-1} + b_f), \quad (3)$$



299 where f_t results in a value between 0 and 1 indicating the degree of information to be forgotten; σ is the logistic
 300 sigmoid function, and W_f, U_f and b_f are trainable parameters. Next, the input gate decides which values will be
 301 updated in the current cell state, and creates a vector of candidate values \tilde{c}_t in the range of (-1, 1) through a \tanh layer,
 302 which will be used to update the current state. With the candidate values calculated from the current state, and the
 303 information conveyed from the forget gate, we can calculate the current cell state as follows:

$$304 \quad i_t = \sigma(W_i x_t + U_i h_{t-1} + b_i), \quad (4)$$

$$305 \quad \tilde{c}_t = \tanh(W_{\tilde{c}} x_t + U_{\tilde{c}} h_{t-1} + b_{\tilde{c}}), \quad (5)$$

$$306 \quad c_t = f_t * c_{t-1} + i_t * \tilde{c}_t, \quad (6)$$

307 where i_t is the input gate that defines which information of \tilde{c}_t will be used to update the current cell state and is in the
 308 range of (0, 1); c_t represents the current cell state; and $W_{\tilde{c}}, U_{\tilde{c}}, b_{\tilde{c}}, W_i, U_i$, and b_i are trainable parameters. Finally, the
 309 output gate o_t controls the information of cell state c_t to a new hidden state h_t , which is computed using the following
 310 equation:

$$311 \quad o_t = \sigma(W_o x_t + U_o h_{t-1} + b_o), \quad (7)$$

$$312 \quad h_t = \tanh(c_t) * o_t, \quad (8)$$

313 With the new hidden state calculated, ET and R_{ECO} can be calculated using a one unit dense layer:

$$314 \quad y_t = W_d h_t + b_d, \quad (9)$$

315 where W_d and b_d are additional trainable parameters. In summary, the LSTM unit calculates the internal state using
 316 current meteorological forcings and remote sensing data at every time step. The forget gate, input gate, and output
 317 gate decide what information from previous time steps will be kept, updated, and conveyed to the new hidden state.
 318 Finally, with a single dense layer, the algorithm will output ET and R_{ECO} estimation from the trained model.

319 A 70%-30% split between training and validation time series data was applied here, where the first 70% of the data
 320 were used for HPM development as a learning process, and 30% of the data were used as validation sets at individual
 321 sites. At the East River Watershed, HPM results were also validated with benchmark CLM outputs from Tran et al.
 322 (2019) and FLUXNET measurements. We used the mean absolute error (MAE), and adjusted R^2 as the statistical
 323 measure to determine model performance.

$$324 \quad MAE = \frac{\sum_{i=1}^n |y_{predict} - y_{measured}|}{n}, \quad (10)$$

$$325 \quad R^2 = 1 - \frac{SSE}{SS}, \quad (11)$$

326 where SSE represents the sum of squared errors, SS is the sum of squares of the response attributes (i.e., ET or R_{ECO}),
 327 and n is the number of data points. In most models, the configuration of the neural networks includes a first LSTM
 328 layer with 50 units, a second LSTM layer with 25 units, and a dense layer with 8 units having L2 regularizers and a
 329 final output dense layer. Dropout layers are also embedded in the model to prevent overfitting. Other configurations



330 of networks may provide better estimation results; however, they are not assessed in this study. More information
331 about the LSTM-RNN method is provided by (Olah, 2015)

332 3.2 Feature Selection

333 Given data availability and the practicability of applying HPM to estimate ET and R_{ECO} at sparsely monitored
334 watersheds, we also selected, constructed, and augmented certain attributes as features for HPM.

335 3.2.1 Snow information

336 In mountainous watersheds, snow dynamics significantly influence water and carbon fluxes. Because of the
337 difficulties in measuring snow time series over space, we did not directly use attributes such as snow water equivalent
338 as input to HPM. Instead, we separated precipitation data into snow precipitation (air temperature < 0) and rainfall
339 precipitation (air temperature > 0). This is in line with what has been used in hydrological models such as CLM
340 (Oleson et al., 2013). Note that for certain sites in this study, snow is not present (e.g., US-Ton). In order to capture
341 the dynamics of snow processes, such as accumulation and melting, we constructed a categorical variable (sn), as
342 follows:

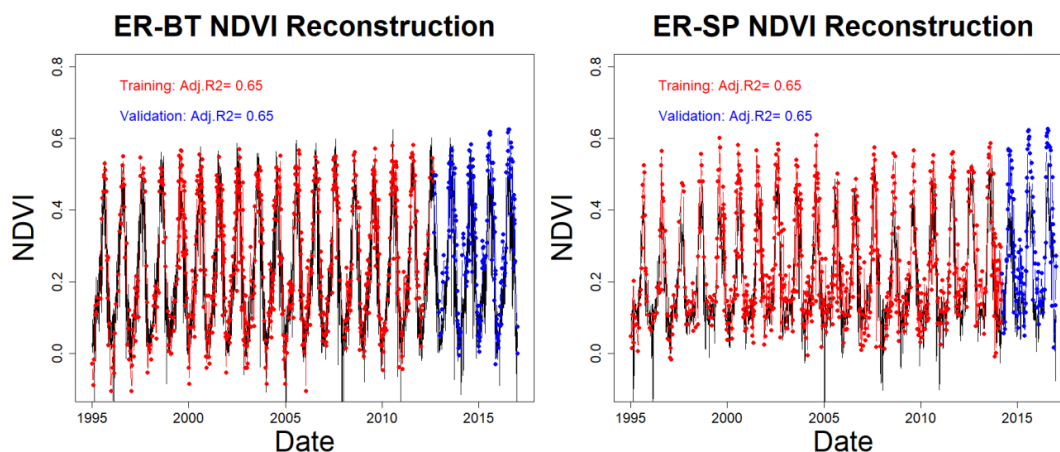
$$343 \quad sn = \begin{cases} 0, & \text{during snow accumulation; } SWE > 0 \text{ and } SWE < \text{peak } SWE \\ 1, & \text{during snow melting; } SWE > 0 \text{ and } SWE \leq \text{peak } SWE \\ 2, & \text{no snow; } SWE = 0 \end{cases}, \quad (12)$$

344 Since data on peak SWE are rarely available because of the difficulties in measuring snow, we also define a
345 proxy categorical variable, sn . When no SWE measurements were available, we estimated sn using air and soil
346 temperature data following Knowles et al. (2016), who found significant correlations between the day of peak snow
347 accumulation and first day of air temperature above 0 degrees Celsius, as follows:

$$348 \quad sn = \begin{cases} 0, & \text{during snow accumulation; Air Temperature } < 0 \\ 1, & \text{during snow melting; Air Temperature } > 0 \text{ while Soil Temperature } \leq 0, \\ 2, & \text{no snow; Air Temperature and Soil Temperature } > 0 \end{cases}, \quad (13)$$

349 3.2.2 Vegetation information

350 To mitigate the long return periods of satellites and the presence of clouds, we reconstructed daily NDVI
351 values based on meteorological forcings data (e.g., air temperature, precipitation, radiation) using deep-learning
352 recurrent neural networks, leading to estimates of NDVI at daily temporal resolution. For example, Figure 4 represents
353 Landsat-derived NDVI and reconstructed NDVI values for two sites at the East River, CO watershed: Butte (ER-BT),
354 and Schofield Pass (ER-SP). Figure 4 reveals that based on meteorological forcings data only, the reconstructions
355 achieved an adjusted R^2 of 0.65. Though not ideal, as satellites continue to advance and more training data becomes
356 available, the accuracy of NDVI temporal reconstruction will increase.



357

358 **Figure 4: Temporal reconstruction of NDVI at ER-BT (left) and ER-SP (right). Black line represents reconstructed daily**
 359 **NDVI. Red points are used for training and blue points are used for validation**

360 **4. Results**

361 We tested HPM’s capabilities using different use cases to explore different conditions. First, we tested the
 362 capability of HPM to estimate long-term temporal dependency among meteorological forcings, ET, and R_{ECO}
 363 (presented in Section 4.1). Second, we validated HPM’s capability to estimate the spatial distribution of ET and R_{ECO}
 364 over space in selected watersheds, where we developed HPM using existing FLUXNET data (data-driven HPM,
 365 Section 4.2) or outputs from a mechanistic model (physical-model-based HPM, Section 4.3). Third, HPM was used
 366 to estimate ET and R_{ECO} at selected sites within the East River Watershed and to distinguish how local factors (e.g.,
 367 vegetation heterogeneity) influence ET and R_{ECO} dynamics (Section 4.4). These four use cases illustrate and
 368 demonstrate how HPM can be developed and applied at target watersheds, where data are sparse.

369 **4.1 Use Case 1: ET and R_{ECO} Time Series Estimation with HPM Developed at FLUXNET Sites**

370 Local HPMs were developed to estimate ET and R_{ECO} using flux tower data obtained from FLUXNET sites
 371 listed in Table 1. Attributes used to train these individual HPM are documented in Table 3.

372

Table 3. Attributes used for HPM development in Use Case 1

| Site ID | Site Name | Attributes |
|---------|---------------------------------|---|
| US-NRI | Niwot Ridge | Air Temperature, precipitation, net radiation, sn, NDVI, soil temperature |
| CA-Oas | Saskatchewan- Aspen | Air Temperature, precipitation, net radiation, sn, NDVI, soil temperature |
| CA-Obs | Saskatchewan- Black Spruce | Air Temperature, precipitation, net radiation, sn, NDVI, soil temperature |
| US-SRM | Santa Rita Mesquite | Air Temperature, precipitation, net radiation, NDVI, soil temperature |
| US-Ton | Tonzi Ranch | Air Temperature, precipitation, net radiation, NDVI, soil temperature |
| US-Var | Vaira Ranch-lone | Air Temperature, precipitation, net radiation, NDVI, soil temperature |
| US-Whs | Walnut Gulch Lucky Hills Shrub | Air Temperature, precipitation, net radiation, NDVI, soil temperature |
| US-Wkg | Walnut Gulch Kendall Grasslands | Air Temperature, precipitation, net radiation, NDVI, soil temperature |

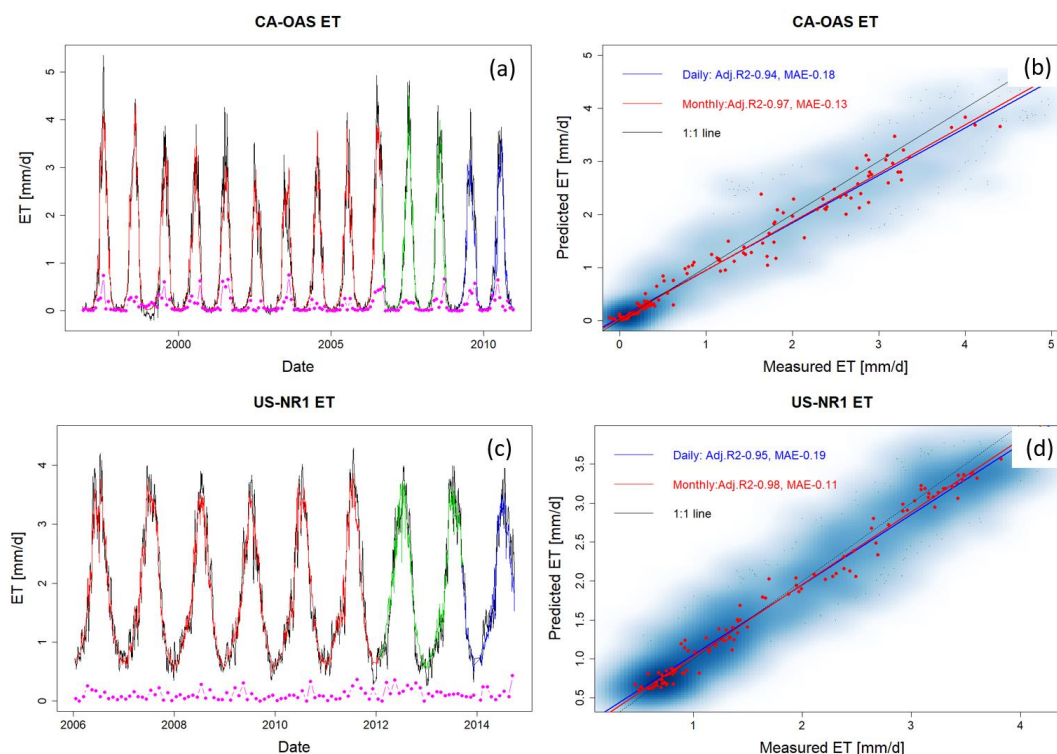
373

374

The results, which are shown in Figure 5 and Table 4, reveal that the HPM approach was effective for
 estimating ET. Adjusted R^2 between the HPM estimates and flux tower measurements are above 0.85 for all sites,



375 and mean absolute errors are small at a level of ~ 0.2 mm/d. Figure 5 displays the estimation of ET from HPM US-
376 NR1 and CA-OAS (other sites provided in supplementary material), and presents monthly mean ET values of
377 measurements, HPM estimations, and differences. The long-term trends in ET are well captured by HPM. At larger
378 temporal scales (monthly or yearly), HPM provides reasonable estimation of ET at these sites. However, short-term
379 fluctuations during the summer are also not well captured by ET, specifically at California sites during the periods
380 when plant transpiration and soil evaporation are constrained by soil moisture (Figure A2 panel a).

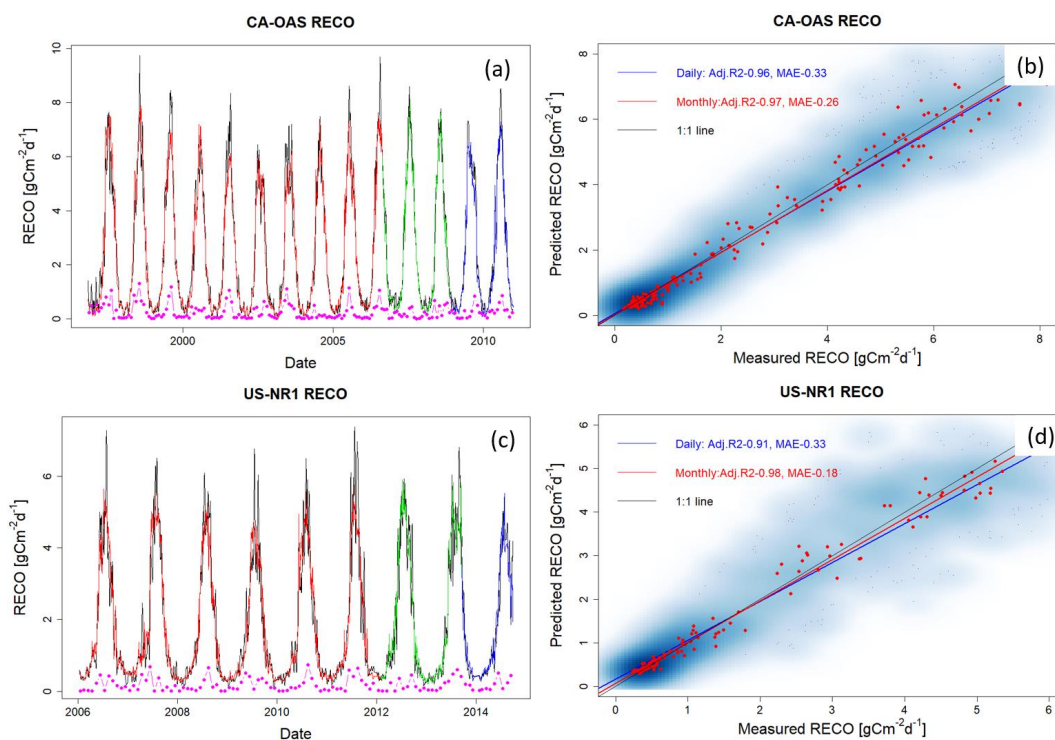


381
382 **Figure 5:** ET estimation with data from FLUXNET sites at CA-OAS and US-NR1. Panels (a) and (c) illustrate the daily
383 estimation of ET with red, green, and blue lines representing data used for training, validation, and prediction, respectively,
384 and the black line showing the eddy covariance measurements. Pink points describe monthly mean difference between
385 HPM estimation and measured data. Panels (b) and (d) show the scatter plots of daily (blue) and monthly (red) ET. Darker
386 blue clouds represent greater density of data points. Results for other sites are included in supplementary materials below
387 (Figures A1 and A2).

388 Similarly, Table 4 and Figure 6 reveal that HPM was also effective in estimating R_{ECO} , leading to small MAE
389 and adjusted R^2 of 0.8 between estimated and measured R_{ECO} except for US-Ton and US-Var. Figure 6 presents HPM-
390 estimated R_{ECO} at US-NR1 and CA-OAS, with other sites presented in Figures A3 and A4. Long-term dynamics of
391 R_{ECO} are also successfully captured by HPM; however, HPM underestimates R_{ECO} during peak growing seasons. For
392 example, at US-NR1, error increased during the growing season, when estimates of R_{ECO} are smaller than measured



393 R_{ECO} . While soil moisture can limit R_{ECO} during peak growing season (Ng et al., 2014; Wang et al., 2014), the
 394 developed HPM does not include soil moisture as a key attribute. As such, HPM underestimates R_{ECO} during peak
 395 growing season, leading to higher MAE than other times of the year. In addition, HPM R_{ECO} estimation at US-Ton
 396 and US-Var show higher uncertainties (i.e., $MAE > 0.4$ and $Adj. R^2 < 0.8$), which also indicates that soil moisture
 397 data is necessary to increase R_{ECO} prediction accuracy in this ecoregion.



398
 399 **Figure 6:** R_{ECO} estimation with data from FLUXNET sites at CA-OAS and US-NR1. Panels (a) and (c) present daily
 400 estimation of R_{ECO} with red, green, and blue lines representing data used for training, validation, and prediction, and the
 401 black line shows the eddy covariance measurements. Pink points describe monthly mean difference between HPM
 402 estimation and measured data. Panels (b) and (d) show the scatter plots of daily (blue) and monthly (red) R_{ECO} . Darker
 403 blue clouds represent greater density of data points. Results for other sites are included in supplementary materials below
 404 (Figures A3 and A4).

405 **Table 4: Statistical measures of HPM estimation of ET and R_{ECO}**

| Site ID | Train MAE -ET [mm/d] | Test MAE -ET [mm/d] | Train Adj. R^2 - ET | Test Adj. R^2 - ET | Train MAE $-R_{ECO}$ [gCm ⁻² d ⁻¹] | Test MAE $-R_{ECO}$ [gCm ⁻² d ⁻¹] | Train Adj. R^2 $-R_{ECO}$ | Test Adj. R^2 $-R_{ECO}$ |
|---------|----------------------|---------------------|-----------------------|----------------------|---|--|-----------------------------|----------------------------|
| US-NR1 | 0.19 | 0.11 | 0.95 | 0.98 | 0.33 | 0.18 | 0.91 | 0.98 |
| CA-Oas | 0.18 | 0.13 | 0.94 | 0.97 | 0.33 | 0.26 | 0.96 | 0.97 |
| CA-Obs | 0.12 | 0.09 | 0.95 | 0.96 | 0.29 | 0.25 | 0.96 | 0.97 |
| US-SRM | 0.22 | 0.17 | 0.92 | 0.94 | 0.24 | 0.19 | 0.80 | 0.87 |
| US-Ton | 0.22 | 0.17 | 0.92 | 0.94 | 0.43 | 0.36 | 0.76 | 0.82 |



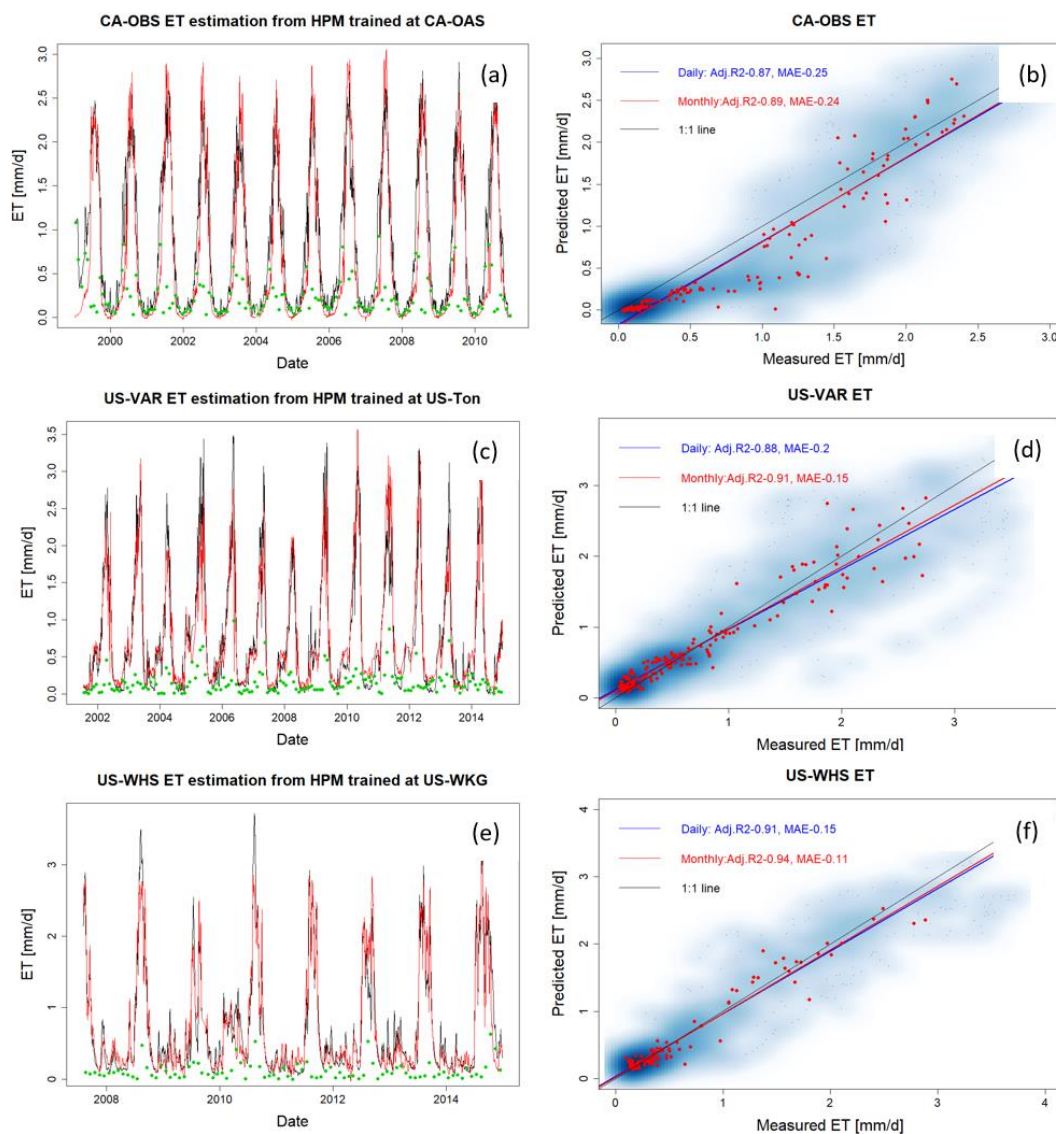
| | | | | | | | | |
|--------|------|------|------|------|------|------|------|------|
| US-Var | 0.15 | 0.12 | 0.92 | 0.95 | 0.49 | 0.38 | 0.81 | 0.88 |
| US-Whs | 0.13 | 0.09 | 0.93 | 0.96 | 0.12 | 0.09 | 0.84 | 0.89 |
| US-Wkg | 0.19 | 0.15 | 0.87 | 0.91 | 0.18 | 0.15 | 0.85 | 0.91 |

406

407 4.2 Use Case 2: Ecoregion-Based, Data-Driven HPM Model for ET and R_{ECO} Estimation

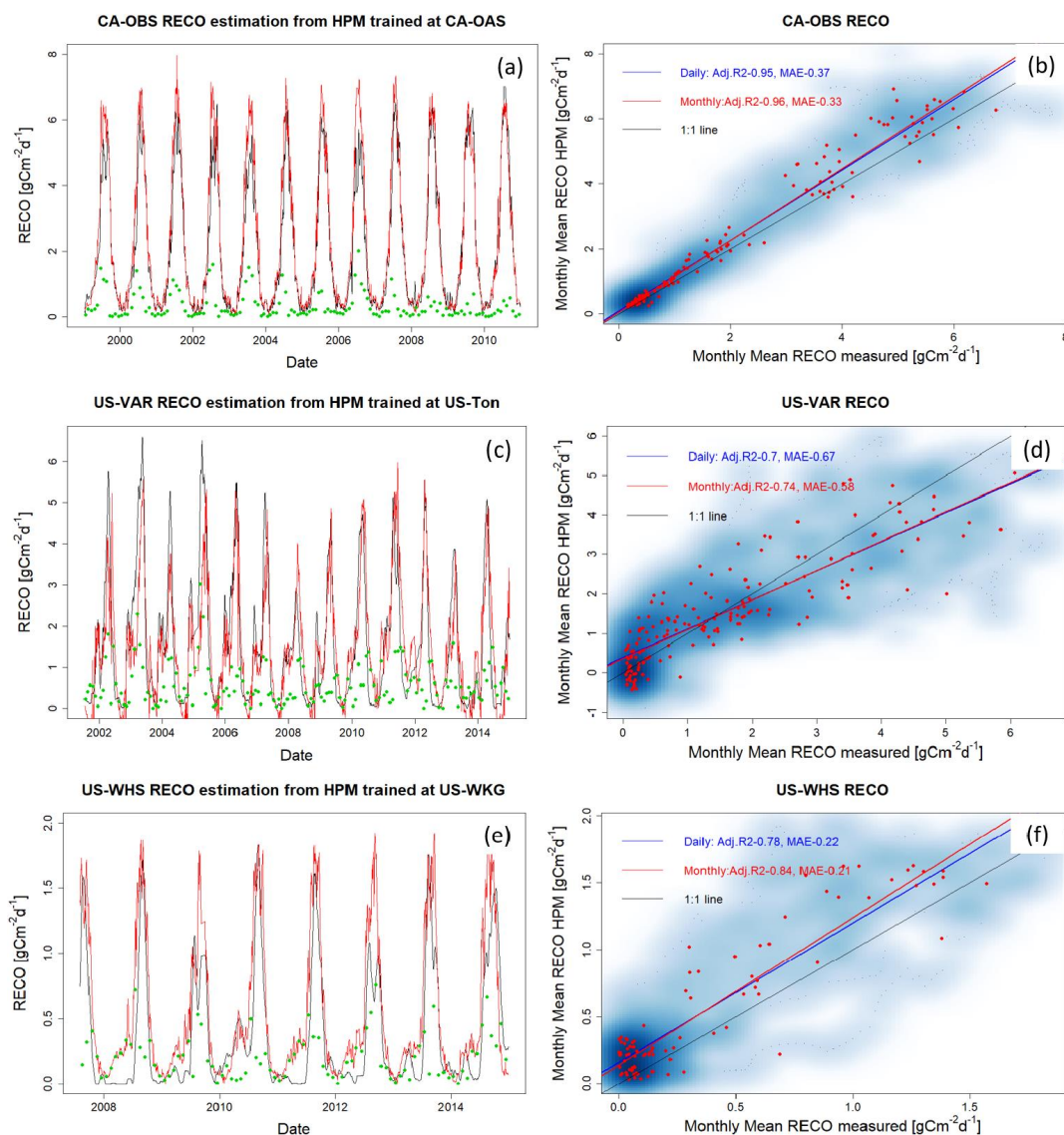
408 While the effort and cost involved in establishing flux towers naturally limit the spatial coverage of obtained
409 measurements, point scale measurements from one FLUXNET station provides representative information about
410 ecosystem dynamics at other locations within the same ecoregion. In this section, we explored the use of a data-driven
411 HPM trained with one FLUXNET station to estimate ET and R_{ECO} at other locations within the same ecoregion. To
412 test this approach, we first trained HPM at a selected FLUXNET stations and validated these HPM models at other
413 FLUXNET stations (ET and R_{ECO} data at testing sites were only used for comparison with HPM prediction) within
414 the same ecoregion. Specifically, we developed HPM models at US-Ton, CA-Oas and US-Wkg, and provided ET and
415 R_{ECO} estimations at US-Var, CA-Obs and US-Whs at three ecoregions, respectively.

416 Table 5 summarizes how we developed the data-driven HPM models for spatially distributed estimation of
417 ET and R_{ECO} as well as the corresponding statistical summaries. The estimation led to an adjusted R^2 greater than
418 0.85 for US-Obs and US-Whs and 0.70 for US-Var. Figures 7 and 8 present the time series of HPM-estimated ET and
419 R_{ECO} compared to measurements from flux towers. The figures show that HPM captures the seasonal and longer-term
420 dynamics of ET and R_{ECO} well, as indicated by the high adjusted R^2 . However, we observed an increased error in
421 HPM-based estimations compared to measurements during peak growing seasons (e.g., a 0.5 mm discrepancy in June
422 mean ET). Higher prediction accuracy for the two ecoregions presented by US-Whs and CA-Obs are observed
423 compared to US-Ton, which indicates other attributes (e.g., soil moisture) are necessary to improve prediction
424 accuracy, especially for sites limited by moisture conditions. Although the prediction accuracy is not as high as Use
425 Case 1 (Section 4.1), this use case demonstrates that HPM can learn the complicated relationships between responses
426 and features successfully, and that a local data-driven HPM can be used to fuse with data from other subsites for long-
427 term estimation of ET and R_{ECO} within the same ecoregions.



428

429 **Figure 7.** ET estimation at CA-Oas (a), US-Var (c), and US-Whs (e) with HPM trained at US-Ton, US-Wkg, and CA-Oas,
430 respectively. Red and black lines represent HPM estimation and real measurements, with green points denoting the monthly
431 mean difference between HPM estimations and measurements. Panels (b), (d), and (f) show the scatter plots of daily (blue)
432 and monthly (red) ET at these three sites. Darker blue clouds represent greater density of data points.



433

434 **Figure 8.** R_{ECO} estimation at CA-Oas (a), US-Var (c), and US-Whs (e) with HPM trained at US-Ton, US-Wkg, and CA-
 435 Oas, respectively. Red and black lines represent HPM estimations and real measurements; green points denote the
 436 monthly mean difference between HPM estimation and measurements. Panels (b), (d), and (f) show the scatter plots of
 437 daily (blue) and monthly (red) R_{ECO} at these three sites. Darker blue clouds represent greater density of data points.

438 **4.3 Use Case 3: Ecoregion-Based, Mechanistic HPM Estimation of ET**

439 Mechanistic HPM, which is trained with ET estimates from 1-D physically-based-model simulations,
 440 provides an avenue for estimating ET in ecoregions where direct measurements from eddy covariance tower are not

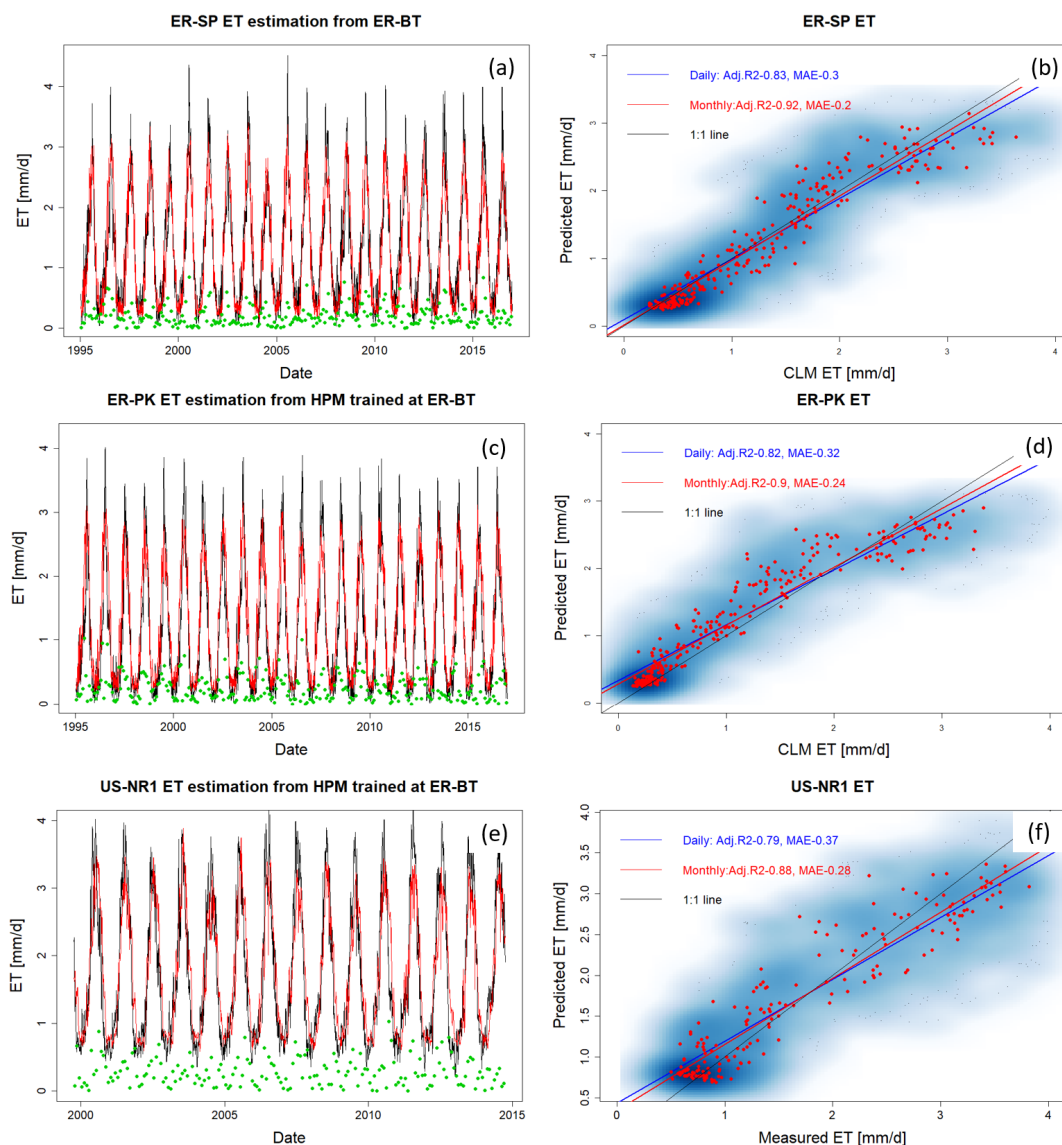


441 available. In order to test the effectiveness of the mechanistic HPM, we focused on the three SNOTEL stations and
 442 US-NR1, which locates in the “Western Cordillera” ecoregion. Mechanistic HPM is coupled with CLM simulations
 443 at these sites (Tran et al., 2019). To ensure the CLM physically-based-model simulations can provide alternative
 444 datasets to develop mechanistic HPMs, we compared CLM estimation and direct measurements of ET at US-NR1
 445 (Figure S2). The consistent results between measured ET and CLM-estimated ET (adjusted $R^2 = 0.88$; $k = 0.95$)
 446 indicate independent CLM simulations can be effectively used to develop the mechanistic HPM.

447 We applied mechanistic HPM trained with 1-D CLM developed at ER-BT (Tran et al., 2019) to estimate ET
 448 at sites classified as part of the same ecoregion (i.e., ER-SP, ER-PK and US-NR1). We then compared ET estimation
 449 from HPM to independent CLM-based ET estimations at ER-SP and ER-PK and to direct measurements at US-NR1.
 450 Figure 9 shows a high consistency between HPM estimation and the validation data. For all scenarios, an adjusted R^2
 451 of 0.8 or greater is observed (Table 5), which strongly indicates that mechanistic HPM can provide accurate ET
 452 estimation at sites of similar ecoregions. These results suggest the broad applicability of mechanistic HPM to estimate
 453 ET based on ecoregion characteristics. This approach is expected to be particularly useful for regions where flux
 454 towers are difficult to install or where measured fluxes are not representative of the landscape, such as in mountainous
 455 watersheds.

456 **Table 5. Statistical summary of HPM estimation over space with FLUXNET sites and SNOTEL stations with CLM**

| Target Site | Training Site | Level II Ecoregion | ET MSE (monthly)[mm/d] | ET Adj. R^2 | R_{ECO} MSE(monthly)[$gCm^{-2}d^{-1}$] | R_{ECO} Adj. R^2 |
|-------------|---------------|------------------------------|------------------------|---------------|--|----------------------|
| CA-Obs | CA-Oas | Boreal Plain | 0.39 | 0.88 | 0.36 | 0.97 |
| US-Var | US-Ton | Mediterranean California | 0.34 | 0.70 | 0.67 | 0.70 |
| US-Whs | US-Wkg | Western Serra Madre Piedmont | 0.13 | 0.94 | 0.17 | 0.85 |
| ER-SP | ER-BT | Western Cordillera | 0.20 | 0.92 | - | - |
| ER-PK | ER-BT | Western Cordillera | 0.24 | 0.90 | - | - |
| US-NR1 | ER-BT | Western Cordillera | 0.23 | 0.90 | - | - |



457

458 **Figure 9.** HPMs trained with CLM simulation at ER-BT are used to estimate ET at ER-SP, ER-PK, and
 459 (a), (c), and (e) display HPM estimation of ET (red lines), as well as independent CLM estimation at ER-SP, ER-PK, and
 460 eddy covariance measurements at US-NR1 (black lines). Panels (b), (d), and (f) show the scatter plots of daily (blue) and
 461 monthly (red) ET at these three sites. Darker blue clouds represent greater density of data points.

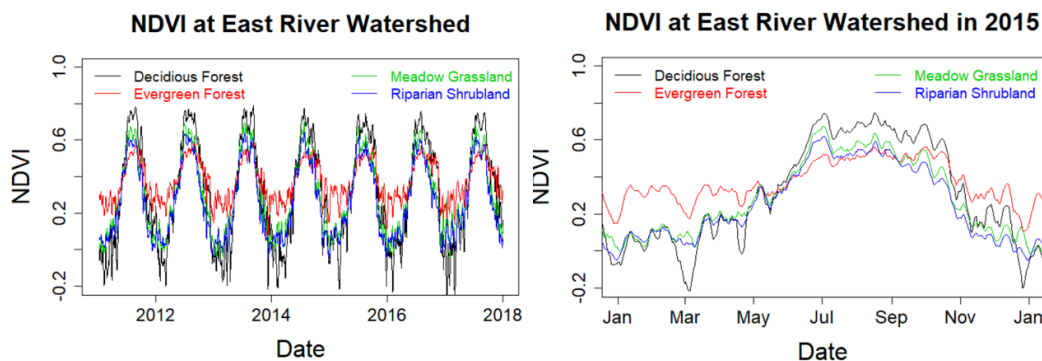
462 **4.4 Exploration of How ET and R_{ECO} Varies with Meteorological forcings and Vegetation Heterogeneity at**
 463 **the East River Watershed**

464 ET and R_{ECO} estimated from the HPM model at the mountainous East River Watershed in CO enabled us to
 465 analyze how vegetation heterogeneity and meteorological forcings heterogeneity influence estimated ET and R_{ECO}



466 dynamics, and to identify limitations in the developed approach for estimating ET and R_{ECO} across mountainous and
467 heterogeneous watersheds.

468 NDVI time-series data provide high-resolution (30m) information about vegetation variability across the East
469 River Watershed. The spatial distribution of vegetation cover presented in Figure 2 (from Falco et al. 2019) enables
470 us to distinguish different patches of deciduous forests, evergreen forests, meadow grassland and riparian shrublands
471 and retrieve corresponding NDVI time-series. Figure 10 shows Landsat-derived and reconstructed NDVI values for
472 the four different vegetation types within the East River Watershed. Evergreen forests have an extended growing
473 season compared to deciduous forests. However, peak NDVI is smaller in evergreen forests compared to deciduous
474 forests. NDVI ranges from 0.2 to 0.6 for evergreen forests, whereas larger fluctuations in NDVI are observed for
475 deciduous forests (-0.2 to 0.8). The NDVI values during the winter are likely sensing both snow and forest density,
476 due to pixel spatial averaging from Landsat images. Similar to Qiao et al. (2016), we also found that the NDVI of
477 deciduous forests exhibits a significant increase during the growing season, followed by a sharp decline (likely caused
478 by defoliation), and that evergreen forests had a more stable NDVI.



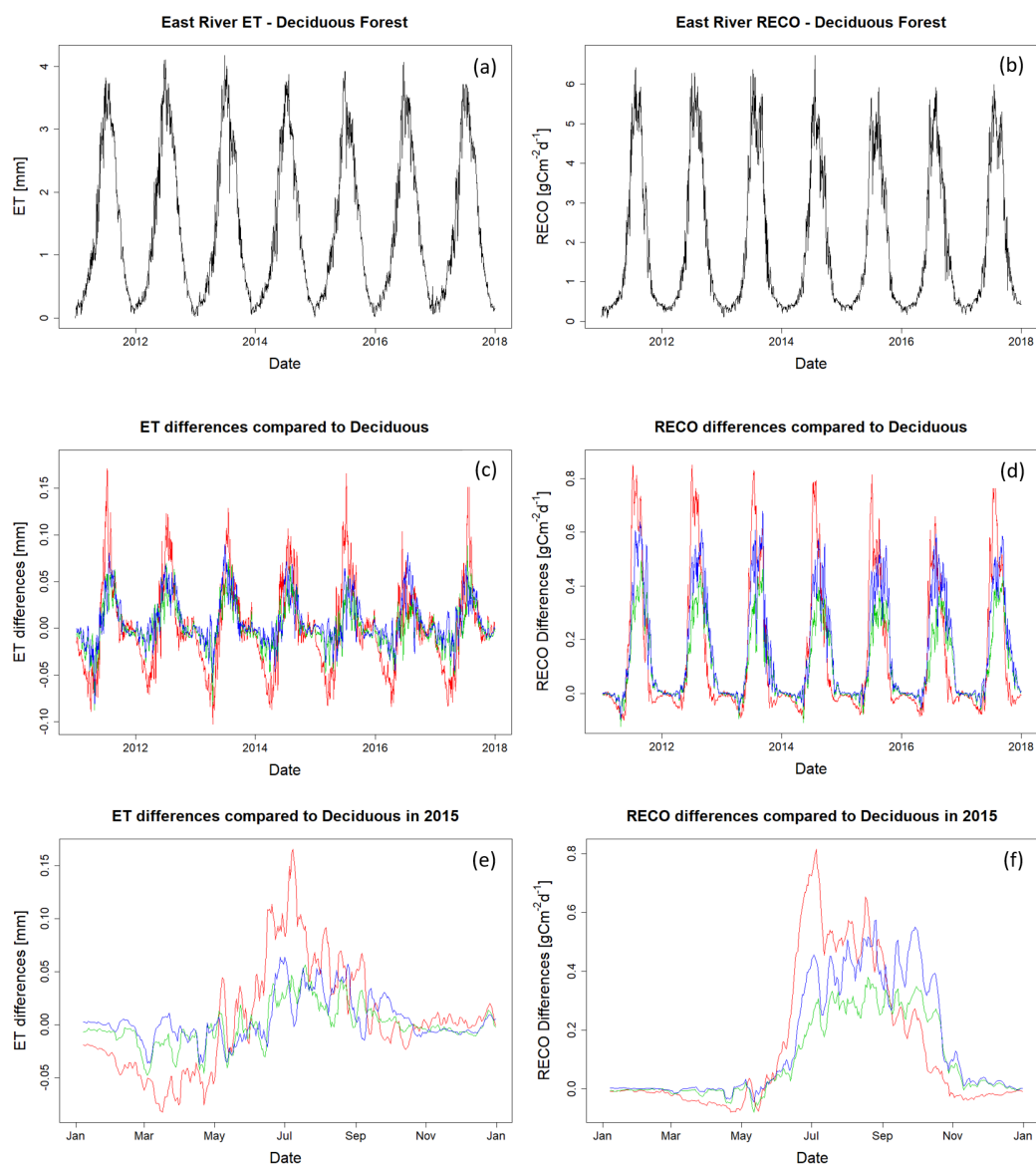
479

480 **Figure 10: Reconstructed NDVI time series at selected locations in the East River Watershed for 2011 to 2018 (panel a) and**
481 **for 2015 (panel b, normal water year). Black, red, green, and blue lines represent the time series of NDVI for deciduous**
482 **forests, meadow grasslands, evergreen forests and riparian shrubland, respectively.**

483 HPM-estimated ET and R_{ECO} also show different dynamics in evergreen forests and deciduous forests. Figure
484 11a and 11b present the time series of estimated ET and R_{ECO} associated with deciduous forests, respectively. Figure
485 11c and d present the ET and R_{ECO} differences between deciduous forests sites and sites with other vegetation (e.g.,
486 evergreen forests shown in red). Before peak growing season, the ET of evergreen forests is about 10% greater than
487 deciduous forests, whereas ET of deciduous forests during peak growing season is greater than evergreen forests.
488 After growing season, the NDVI of deciduous forests is less than 0.2 (loss of leaves) compared to the NDVI of
489 evergreen forests. Before peak growing season, R_{ECO} of evergreen forests is slightly greater than deciduous forests.
490 During peak growing season, R_{ECO} of deciduous forests is around 17% greater than R_{ECO} of evergreen forests. Total
491 annual ET between evergreen and deciduous forests is very close (DF1: 535 to 573 mm and EF1: 532 to 569 mm
492 across 7 years in this study). Total annual R_{ECO} of evergreen forests is smaller than deciduous forests (DF1: 642 to



493 $698 \text{ gCm}^{-2}\text{d}^{-1}$ and EF1: 592 to 639 gCm^{-2}). The ET estimation at East River Watershed is comparable to Mu et al.
494 (2013), where ET is computed based upon the logic of the Penman-Monteith equation and MODIS remote sensing
495 data. At the East River Watershed, data retrieved from Mu et al. (2013) indicate annual ET ranges from 554 to 585
496 mm at deciduous forests sites and 540 to 593 mm at evergreen forests sites. The R^2 between 8-day aggregated HPM-
497 based ET estimation and data retrieved from Mu et al. (2013) achieves 0.65 (Figure S1). Berryman et al. (2018)
498 developed a random forest model to predict growing season soil respiration at subalpine forests in the Southern Rocky
499 Mountain ecoregions. Their results suggest a consistent respiration rate from 2004 to 2006, with 150-day sums of
500 542.8 , 544.3 and 536.5 gCm^{-2} , respectively, with a mean measured growing season respiration across sites and
501 years of 3.37 gCm^{-2} . HPM-based R_{ECO} estimation is also comparable to what Berryman et al. (2018) discovered,
502 with growing season R_{ECO} ranging between 555 to 607 gCm^{-2} and mean growing season R_{ECO} ranging between
503 3.01 to 3.30 gCm^{-2} . While we currently do not have a time-series measurement of ET and R_{ECO} at the East River
504 Watershed for validation, our results are comparable to other studies that focus on sites within the same ecoregion
505 (e.g., Berryman et al., 2018).



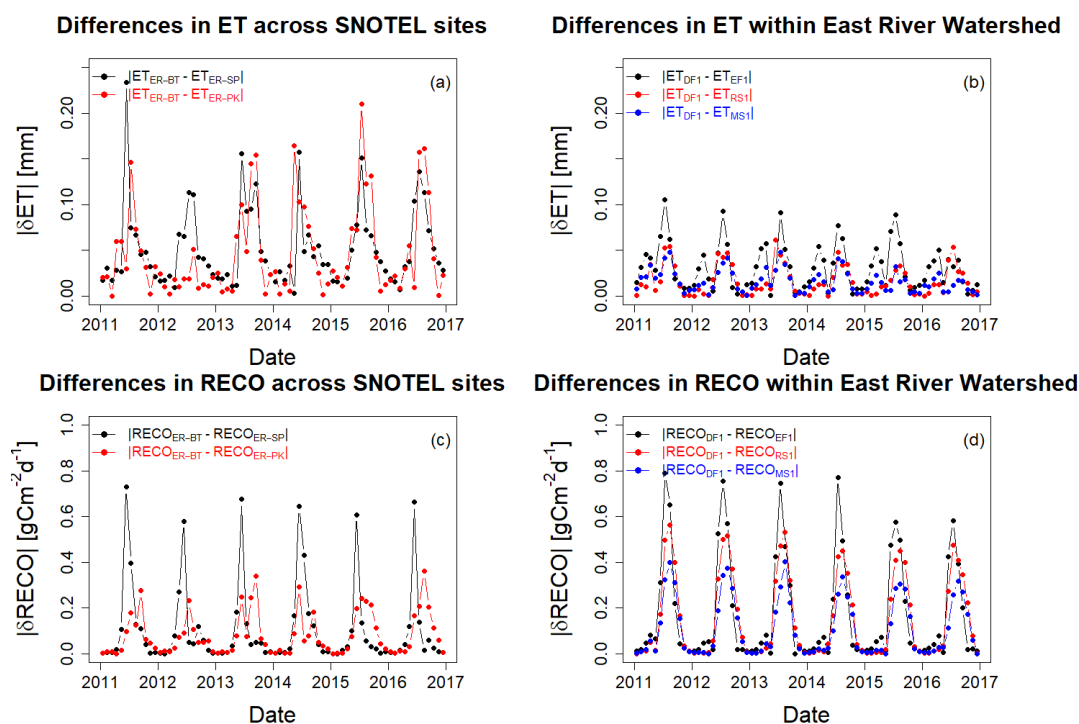
506

507 **Figure 11: ET (a) and R_{ECO} (b) estimation for the deciduous forest site DF1 at the East River Watershed. Panels (c) and (d)**
508 **show the differences in ET and R_{ECO} among various vegetation types and DF1. Red, green, and blue lines represent the**
509 **differences in evergreen forest, meadow, and riparian shrubland compared to DF1. Panels (e) and (f) zoom into 2015 to**
510 **better display seasonal variations.**

511 ET and R_{ECO} estimation at the East River Watershed from the HPM model further enabled us to assess the
512 impacts of small-scale (e.g., hillslope scale) heterogeneity in vegetation type on ET and R_{ECO} dynamics. Figure 12



513 shows the absolute value of monthly mean difference in ET (Fig. 12a and Fig. 12b) and R_{ECO} (Fig. 12c and Fig. 12d)
 514 across SNOTEL stations (ER-BT, ER-SP and ER-PK) and within selected East River locations. A comparison of
 515 meteorological forcings data within selected East River locations and across SNOTEL stations are given in Figure S3.
 516 We observed 2.5 times greater differences in ET across SNOTEL stations compared to the sites within the East River
 517 watershed, whereas the differences in R_{ECO} across SNOTEL stations are at the same level compared to the sites within
 518 East River Watershed (around 0.8 gCm^{-2}). This result indicates small-scale meteorological forcings and vegetation
 519 heterogeneity are the major controls of differences in ET and R_{ECO} at the East River Watershed.



520

521 **Figure 12. Absolute differences in monthly mean ET and R_{ECO} across SNOTEL stations and within East River Watershed.**
 522 **Panels (a) and (c) describe the absolute differences in monthly mean ET and R_{ECO} between ER-BT, ER-SP, and ER-PK.**
 523 **Panels (b) and (d) describe the absolute differences in monthly mean ET and R_{ECO} within East River Watershed**
 524 **between deciduous forest (DF1), evergreen forest (EF1), meadow (MS1), and riparian shrubland (RS1).**

525 5. Discussion

526 Our study demonstrates that HPM provides reliable estimations of ET and R_{ECO} under various climate and
 527 vegetation conditions, including data-based HPMs that are trained with FLUXNET data and physical-model-based
 528 HPMs that are coupled with simulations results from mechanistic models (i.e., CLM in our case). With 70% of the
 529 data used for training (model development), ET and R_{ECO} estimation from HPM achieves an adjusted R^2 of 0.9
 530 compared to eddy covariance measurements. With this high estimation accuracy, we demonstrated that this approach



531 could be used for predicting ET and R_{ECO} over time. HPM is capable of “learning” the complex interactions among
532 meteorological forcings, vegetation dynamics, and water and carbon fluxes. The underlying relationships acquired by
533 HPM can serve as a local ecohydrological model for long-term monitoring of ET and R_{ECO} , with the aid of remote
534 sensing data, and can fill in gap data during occasional equipment failure.

535 HPM was also successful at estimating the spatial distribution of ET and R_{ECO} through exploiting an
536 ecoregion concept. Using the representative FLUXNET sites in different ecoregions, HPM provided estimates of ET
537 and R_{ECO} at locations using learned relationships from other sites having the same ecoregion classification. For
538 conditions where no FLUXNET sites are within the same ecoregion, our study showed that physically-based models
539 that can utilize weather forcings data can provide alternatives for developing mechanistic HPM to estimate ET and
540 R_{ECO} . We found that HPM performance was more reliable when trained and applied at different watersheds in the
541 same ecoregion. For example, HPM that only relies on energy-related parameters was able to successfully estimate
542 ET and R_{ECO} at US-NR1 and CA-OAS, where radiation and temperature are key components that regulate ET and
543 R_{ECO} dynamics. However, HPM with the same input features do not yield desired results at sites limited by water
544 conditions (e.g., US-Ton and US-Var), due to lack of soil moisture data. This change indicates that parameter
545 optimization and attributes selection may be needed for sites that are limited by moisture conditions, because important
546 features can be subject to local conditions that potentially lower HPM performance.

547 We confirmed the important role of small-scale vegetation heterogeneity in modeling ET and R_{ECO} dynamics,
548 which further enabled us to better understand ecosystem dynamics at the East River Watershed. As indicated from
549 NDVI time series (Fig 10), evergreen forests have a longer growing season compared to deciduous forests; however,
550 deciduous forests have greater peak NDVI values. Correspondingly, we also observed an earlier increase in ET and
551 R_{ECO} for evergreen forests (before May), but larger ET and R_{ECO} for deciduous forests during peak growing season
552 (around June and July). Annual ET between deciduous forests and evergreen forests are not statistically different,
553 which is similar to (Berryman et al., 2018; Mu et al., 2013). Annual R_{ECO} differences between evergreen forests and
554 deciduous forests are around 50 gCm^{-2} , which is comparable to Berryman et al. (2018). Similar dynamics were also
555 observed at regions that have different climate conditions. Through assessing the differential mechanisms of
556 deciduous forests and evergreen forests at various sites under Mediterranean climates, Baldocchi et al. (2010) found
557 that deciduous forests had a shorter growing season, but showed a greater capacity for assimilating carbon during the
558 growing season. Evergreen forests, on the other hand, had an extended growing season but with a smaller capacity for
559 gaining carbon. These results were identified through analyzing the relationships among leaf ages, leaf nitrogen level,
560 leaf area, and water use efficiencies of these tree species at the selected Mediterranean sites. Older leaves tend to have
561 smaller leaf nitrogen and stomata conductance, and thus evergreen forest ET and R_{ECO} are smaller during the peak
562 growing season compared to deciduous forests, yet maintain a relatively high level before the peak growing season or
563 during defoliation. Hu et al. (2010) analyzed flux data at US-NR1 to determine the relationships between growing
564 season lengths and carbon sequestration, and found that extended growing season length resulted in less annual CO_2
565 uptake. They also found that the duration of growing seasons substantially decreases snow water storage, which
566 significantly decreases forest carbon uptake. While we were not able in this study to assess the differential advantages



567 and physiological mechanisms among vegetation types, HPM-based estimation of ET and R_{ECO} presented similar
568 dynamic trends to those found in Berryman et al. (2018); Hu et al. (2018); and Mu et al. (2013).

569 Microclimate and small-scale heterogeneity in meteorological forcings attributes control the magnitude and
570 timing of ET and R_{ECO} dynamics. For example, other field observations along the Rocky Mountain ranges have shown
571 that south-facing hillslopes have significantly earlier snowmelt compared to north-facing hillslopes (Kampf et al.,
572 2015; Webb et al., 2018), which are hypothesized to result in significant differences in ET and R_{ECO} dynamics. As a
573 result, estimation of small-scale ET and R_{ECO} dynamics requires high spatial resolution meteorological inputs, which
574 is currently a challenge. We originally intended to investigate aspect impacts on ET and R_{ECO} dynamics at East River
575 Watershed by selecting East River sites with different slope orientations. However, small-scale meteorological-
576 forcings heterogeneity and microclimate were not available due to the relatively low spatial resolution of
577 meteorological forcings inputs (DAYMET, 1 km scale). While DAYMET data suggest that differences in air
578 temperature and solar radiation are very small for sites located at different portions of the watershed, the three weather
579 stations at the site reveal that spatial heterogeneity in meteorological forcing attributes do exist, especially air
580 temperature (Figure S4). Even though the small-scale meteorological forcings heterogeneity is partly embedded in
581 NDVI time series, the heterogeneity in ET and R_{ECO} estimated from HPM at the East River Watershed is potentially
582 underestimated, due to the insufficient spatial resolution of meteorological inputs. In addition to limitations imposed
583 from the spatial resolution, uncertainties in meteorological inputs can also result in large errors (i.e., >20% MAE) and
584 reduce accuracy by 10-30% in ET and R_{ECO} estimations as suggested by Mu et al. (2013) and Zhang et al. (2019).
585 Thus, there is still a significant need for high-spatial-resolution meteorological-forcing data products, such as data
586 provided by the Surface Atmosphere Integrated Field Laboratory (SAIL) that can capture small-scale heterogeneity
587 for implementing into HPM, which will then enable us to better assess the governing factors that regulate small-scale
588 heterogeneity in ET and R_{ECO} .

589 In addition to the quality of meteorological data, HPM is also influenced by remote sensing inputs accuracy.
590 Incorrectly calculated or pixel-averaged NDVI values from Landsat images can greatly alter HPM outputs for ET and
591 R_{ECO} . Satellite images with different cloud cover have a slight influence over the NDVI values calculated, which do
592 not represent real-time vegetation conditions. Algorithms used to reconstruct daily NDVI time series are also subject
593 to uncertainties. However, with recent advances in remote sensing and satellite technologies (McCabe et al., 2017),
594 the spatial and temporal resolution should greatly increase in the future (i.e., 3 m resolution and daily). These advances
595 will lead to more accurate classification of vegetation types and NDVI calculations, which are expected to decrease
596 uncertainty associated with flux estimation

597 Another source of uncertainty in HPM arises from the choice of hybrid approaches and any parameter
598 uncertainties in mechanistic models. Since HPM relies on accurate ET and R_{ECO} inputs from flux towers or
599 mechanistic models, any uncertainties in measuring or modeling ET and R_{ECO} will propagate to HPM. If HPM is
600 developed with a mechanistic model that has such missing components, these biases will be passed on to HPM
601 estimation of ET and R_{ECO} . Parameter and conceptual model uncertainties in mechanistic models also restrict HPM's
602 ability to "learn" the ecosystem dynamics. In order to reduce potential biasedness, we trained data-based HPM and



603 physical-model-based HPM upon long time series (e.g., > 5 years) with quality assessed data or simulation results,
604 which also enables HPM to better memorize long time dependencies of ecosystem dynamics. Though the
605 quantification of uncertainties remains challenging, efforts have been made to lower these uncertainties using the
606 technical advances described here.

607 **6. Conclusion**

608 In this study, we developed and tested a Hybrid Predictive Modeling (HPM) approach for ET and R_{ECO}
609 estimation, with a focus on mountainous watersheds. We developed individual HPM models at various FLUXNET
610 sites and at sites where data can supports the proper development of a mechanistic model (e.g., CLM). These models
611 were validated against eddy covariance measurements and CLM outputs. We further used these models for ET and
612 R_{ECO} estimation at watersheds within the same ecoregion to test HPM's capability of providing estimation over space,
613 where only meteorological forcings data and remote sensing data were available. Lastly, we applied the HPM to
614 provide long-term estimation of ET and R_{ECO} and test the sensitivity of HPM to various vegetation types at various
615 sites within the East River Watershed.

616 Given the promising results of HPM, this work offers an avenue for estimating ET and R_{ECO} using easy-to-
617 acquire or commonly available datasets. This study also suggests that the spatial heterogeneity of meteorological
618 forcings and vegetation dynamics have significant impacts on ET and R_{ECO} dynamics, which may be currently
619 underestimated due to typically coarse spatial resolution of data inputs. Parameters related to energy and soil moisture
620 conditions can be implemented into HPM to increase HPM's accuracy, especially for sites limited by soil moisture
621 conditions. Lastly, it should be pointed out that HPM is not restricted to estimation of ET and R_{ECO} only. We focused
622 here on developing HPM for ET and R_{ECO} , but HPM also has great potential for estimating other parameters important
623 for water and carbon cycles. Indeed, other attributes, such as GPP and sensible heat flux, might also be accurately
624 captured and represented with HPM, given the right choice of features.

625 **Data availability.** The data used in this study are from publicly available datasets. FLUXNET measurements can be
626 accessed at <https://FLUXNET.fluxdata.org>. SNOTEL data are available at <https://www.wcc.nrcs.usda.gov/snow/>.
627 DAYMET data can be found at (Thornton et al., 2017) or via Google Earth Engine. Landsat data are available on
628 Google Earth Engine. All data and simulated results associated with this article can be found at [https://data.ess-
629 dive.lbl.gov/view/doi:10.15485/1633810](https://data.ess-dive.lbl.gov/view/doi:10.15485/1633810).

630 **Acknowledgement.** This material is based upon work supported as part of the Watershed Function Scientific Focus
631 Area funded by the U.S. Department of Energy, Office of Science, Office of Biological and Environmental Research
632 under Award Number DE-AC02-05CH11231. We thank Haruko Wainwright and Bhavna Arora for providing
633 comments on East River estimations. We also greatly appreciate all the guidance provided by Professor Yoram Rubin
634 and Professor Dennis Baldocchi at UC Berkeley to the first author. We also acknowledge the Jane Lewis Fellowship
635 Committee of the UC Berkeley for providing fellowship support to the first author.

636 **References**



- 637 Abatzoglou, J. T., Barbero, R., Wolf, J. W. and Holden, Z. A.: Tracking Interannual Streamflow Variability with
638 Drought Indices in the U.S. Pacific Northwest, *J. Hydrometeorol.*, doi:10.1175/jhm-d-13-0167.1, 2014.
- 639 Ai, J., Jia, G., Epstein, H. E., Wang, H., Zhang, A. and Hu, Y.: MODIS-Based Estimates of Global Terrestrial
640 Ecosystem Respiration, *J. Geophys. Res. Biogeosciences*, 123(2), 326–352, doi:10.1002/2017JG004107, 2018.
- 641 Allen, R. G., Pereira, L. S., Raes, D. and Smith, M.: Crop evapotranspiration: Guidelines for computing crop
642 requirements., 1998.
- 643 Anderson, M. C., Allen, R. G., Morse, A. and Kustas, W. P.: Use of Landsat thermal imagery in monitoring
644 evapotranspiration and managing water resources, *Remote Sens. Environ.*, doi:10.1016/j.rse.2011.08.025, 2012.
- 645 Baldocchi, D.: Measuring fluxes of trace gases and energy between ecosystems and the atmosphere - the state and
646 future of the eddy covariance method, *Glob. Chang. Biol.*, doi:10.1111/gcb.12649, 2014.
- 647 Baldocchi, D. D., Ma, S., Rambal, S., Misson, L., Ourcival, J. M., Limousin, J. M., Pereira, J. and Papale, D.: On the
648 differential advantages of evergreenness and deciduousness in mediterranean oak woodlands: A flux perspective, *Ecol.
649 Appl.*, 20(6), 1583–1597, doi:10.1890/08-2047.1, 2010.
- 650 Berryman, E. M., Vanderhoof, M. K., Bradford, J. B., Hawbaker, T. J., Henne, P. D., Burns, S. P., Frank, J. M.,
651 Birdsey, R. A. and Ryan, M. G.: Estimating Soil Respiration in a Subalpine Landscape Using Point, Terrain, Climate,
652 and Greenness Data, *J. Geophys. Res. Biogeosciences*, 123(10), 3231–3249, doi:10.1029/2018JG004613, 2018.
- 653 Bodesheim, P., Jung, M., Gans, F., Mahecha, M. D. and Reichstein, M.: Upscaled diurnal cycles of land-Atmosphere
654 fluxes: A new global half-hourly data product, *Earth Syst. Sci. Data*, 10(3), 1327–1365, doi:10.5194/essd-10-1327-
655 2018, 2018.
- 656 Breshears, D. D., Cobb, N. S., Rich, P. M., Price, K. P., Allen, C. D., Balice, R. G., Romme, W. H., Kastens, J. H.,
657 Floyd, M. L., Belnap, J., Anderson, J. J., Myers, O. B. and Meyer, C. W.: Regional vegetation die-off in response to
658 global-change-type drought, *Proc. Natl. Acad. Sci. U. S. A.*, doi:10.1073/pnas.0505734102, 2005.
- 659 De Bruin, H. A. R.: A model for the Priestley-Taylor parameter alpha., *J. Clim. Appl. Meteorol.*, doi:10.1175/1520-
660 0450(1983)0222.0.CO;2, 1983.
- 661 Budyko, M. I.: The Heat Balance of the Earth's Surface, *Sov. Geogr.*, 2(4), 3–13,
662 doi:10.1080/00385417.1961.10770761, 1961.
- 663 Cox, P. M., Betts, R. A., Jones, C. D., Spall, S. A. and Totterdell, I. J.: Acceleration of global warming due to carbon-
664 cycle feedbacks in a coupled climate model, *Nature*, doi:10.1038/35041539, 2000.
- 665 Dagers, T. D., Kromkamp, J. C., Herman, P. M. J. and van der Wal, D.: A model to assess microphytobenthic primary
666 production in tidal systems using satellite remote sensing, *Remote Sens. Environ.*, 211(April), 129–145,
667 doi:10.1016/j.rse.2018.03.037, 2018.
- 668 Ernakovich, J. G., Hopping, K. A., Berdanier, A. B., Simpson, R. T., Kachergis, E. J., Steltzer, H. and Wallenstein,
669 M. D.: Predicted responses of arctic and alpine ecosystems to altered seasonality under climate change, *Glob. Chang.
670 Biol.*, doi:10.1111/gcb.12568, 2014.
- 671 Falco, N., Wainwright, H., Dafflon, B., Léger, E., Peterson, J., Steltzer, H., Wilmer, C., Rowland, J. C., Williams, K.
672 H. and Hubbard, S. S.: Investigating Microtopographic and Soil Controls on a Mountainous Meadow Plant
673 Community Using High-Resolution Remote Sensing and Surface Geophysical Data., 2019.
- 674 Gao, X., Mei, X., Gu, F., Hao, W., Li, H. and Gong, D.: Ecosystem respiration and its components in a rainfed spring
675 maize cropland in the Loess Plateau, China, *Sci. Rep.*, doi:10.1038/s41598-017-17866-1, 2017.
- 676 Gao, Y., Yu, G., Li, S., Yan, H., Zhu, X., Wang, Q., Shi, P., Zhao, L., Li, Y., Zhang, F., Wang, Y. and Zhang, J.: A
677 remote sensing model to estimate ecosystem respiration in Northern China and the Tibetan Plateau, *Ecol. Modell.*,
678 doi:10.1016/j.ecolmodel.2015.03.001, 2015.
- 679 van Gorsel, E., Delpierre, N., Leuning, R., Black, A., Munger, J. W., Wofsy, S., Aubinet, M., Feigenwinter, C.,
680 Beringer, J., Bonal, D., Chen, B., Chen, J., Clement, R., Davis, K. J., Desai, A. R., Dragoni, D., Etzold, S., Grünwald,



- 681 T., Gu, L., Heinesch, B., Hutyra, L. R., Jans, W. W. P., Kutsch, W., Law, B. E., Leclerc, M. Y., Mammarella, I.,
682 Montagnani, L., Noormets, A., Rebmann, C. and Wharton, S.: Estimating nocturnal ecosystem respiration from the
683 vertical turbulent flux and change in storage of CO₂, *Agric. For. Meteorol.*, 149(11), 1919–1930,
684 doi:10.1016/j.agrformet.2009.06.020, 2009.
- 685 Greve, P., Gudmundsson, L., Orlowsky, B. and Seneviratne, S. I.: Introducing a probabilistic Budyko framework,
686 *Geophys. Res. Lett.*, 42(7), 2261–2269, doi:10.1002/2015GL063449, 2015.
- 687 Hargrove, W. W. and Hoffman, F. M.: Using multivariate clustering to characterize ecoregion borders, *Comput. Sci.*
688 *Eng.*, 1(4), 18–25, doi:10.1109/5992.774837, 1999.
- 689 Hargrove, W. W., Hoffman, F. M. and Law, B. E.: New analysis reveals representativeness of the amerflux network,
690 *Eos (Washington, DC)*, 84(48), doi:10.1029/2003EO480001, 2003.
- 691 Hochreiter, S. and Schmidhuber, J.: Long Short-Term Memory, *Neural Comput.*, doi:10.1162/neco.1997.9.8.1735,
692 1997.
- 693 Homer, C., Dewitz, J., Yang, L., Jin, S., Danielson, P., Xian, G., Coulston, J., Herold, N., Wickham, J. and Megown,
694 K.: Completion of the 2011 national land cover database for the conterminous United States – Representing a decade
695 of land cover change information, *Photogramm. Eng. Remote Sensing*, doi:10.1016/S0099-1112(15)30100-2, 2015.
- 696 Hu, J., Moore, D. J. P., Burns, S. P. and Monson, R.: Longer growing seasons lead to less carbon sequestration by a
697 subalpine forest, *Glob. Chang. Biol.*, 16(2), 771–783, doi:10.1111/j.1365-2486.2009.01967.x, 2010.
- 698 Hu, Z., Wang, G., Sun, X., Zhu, M., Song, C., Huang, K. and Chen, X.: Spatial-Temporal Patterns of
699 Evapotranspiration Along an Elevation Gradient on Mount Gongga, Southwest China, *Water Resour. Res.*,
700 doi:10.1029/2018WR022645, 2018.
- 701 Hubbard, S. S., Williams, K. H., Agarwal, D., Banfield, J., Beller, H., Bouskill, N., Brodie, E., Carroll, R., Dafflon,
702 B., Dwivedi, D., Falco, N., Faybishenko, B., Maxwell, R., Nico, P., Steefel, C., Steltzer, H., Tokunaga, T., Tran, P.
703 A., Wainwright, H. and Varadharajan, C.: The East River, Colorado, Watershed: A Mountainous Community Tested
704 for Improving Predictive Understanding of Multiscale Hydrological–Biogeochemical Dynamics, *Vadose Zo. J.*, 17(1),
705 0, doi:10.2136/vzj2018.03.0061, 2018.
- 706 Immerzeel, W. W., Lutz, A. F., Andrade, M., Bahl, A., Biemans, H., Bolch, T., Hyde, S., Brumby, S., Davies, B. J.,
707 Elmore, A. C., Emmer, A., Feng, M., Fernández, A., Haritashya, U., Kargel, J. S., Koppes, M., Kraaijenbrink, P. D.
708 A., Kulkarni, A. V., Mayewski, P., Nepal, S., Pacheco, P., Painter, T. H., Pellicciotti, F., Rajaram, H., Rupper, S.,
709 Sinisalo, A., Shrestha, A. B., Viviroli, D., Wada, Y., Xiao, C., Yao, T. and Baillie, J. E. M.: Importance and
710 vulnerability of the world’s water towers, *Nat.* (in Press.), 577(May 2019), 1–43, doi:10.1038/s41586-019-1822-y,
711 2019.
- 712 IPCC: IPCC 2019- Special report on climate change, desertification, land degradation, sustainable land management,
713 food security, and greenhouse gas fluxes in terrestrial ecosystem, *Res. Handb. Clim. Chang. Agric. Law*,
714 doi:10.4337/9781784710644, 2019.
- 715 Irons, J. R., Dwyer, J. L. and Barsi, J. A.: The next Landsat satellite: The Landsat Data Continuity Mission, *Remote*
716 *Sens. Environ.*, doi:10.1016/j.rse.2011.08.026, 2012.
- 717 Jägermeyr, J., Gerten, D., Lucht, W., Hostert, P., Migliavacca, M. and Nemani, R.: A high-resolution approach to
718 estimating ecosystem respiration at continental scales using operational satellite data, *Glob. Chang. Biol.*,
719 doi:10.1111/gcb.12443, 2014.
- 720 Jung, M., Reichstein, M., Ciais, P., Seneviratne, S. I., Sheffield, J., Goulden, M. L., Bonan, G., Cescatti, A., Chen, J.,
721 De Jeu, R., Dolman, A. J., Eugster, W., Gerten, D., Gianelle, D., Gobron, N., Heinke, J., Kimball, J., Law, B. E.,
722 Montagnani, L., Mu, Q., Mueller, B., Oleson, K., Papale, D., Richardson, A. D., Rouspard, O., Running, S., Tomelleri,
723 E., Viovy, N., Weber, U., Williams, C., Wood, E., Zaehle, S. and Zhang, K.: Recent decline in the global land
724 evapotranspiration trend due to limited moisture supply, *Nature*, doi:10.1038/nature09396, 2010.
- 725 Jung, M., Reichstein, M., Schwalm, C. R., Huntingford, C., Sitch, S., Ahlström, A., Arneth, A., Camps-Valls, G.,
726 Ciais, P., Friedlingstein, P., Gans, F., Ichii, K., Jain, A. K., Kato, E., Papale, D., Poulter, B., Raduly, B., Rödenbeck,



- 727 C., Tramontana, G., Viovy, N., Wang, Y. P., Weber, U., Zaehle, S. and Zeng, N.: Compensatory water effects link
728 yearly global land CO₂ sink changes to temperature, *Nature*, 541(7638), 516–520, doi:10.1038/nature20780, 2017.
- 729 Kampf, S., Markus, J., Heath, J. and Moore, C.: Snowmelt runoff and soil moisture dynamics on steep subalpine
730 hillslopes, *Hydrol. Process.*, 29(5), 712–723, doi:10.1002/hyp.10179, 2015.
- 731 Keenan, T. F., Migliavacca, M., Papale, D., Baldocchi, D., Reichstein, M., Torn, M. and Wutzler, T.: Widespread
732 inhibition of daytime ecosystem respiration, *Nat. Ecol. Evol.*, 3(3), 407–415, doi:10.1038/s41559-019-0809-2, 2019.
- 733 Knowles, J. F., Burns, S. P., Blanken, P. D. and Monson, R. K.: Fluxes of energy, water, and carbon dioxide from
734 mountain ecosystems at Niwot Ridge, Colorado, *Plant Ecol. Divers.*, doi:10.1080/17550874.2014.904950, 2015.
- 735 Knowles, J. F., Blanken, P. D. and Williams, M. W.: Wet meadow ecosystems contribute the majority of overwinter
736 soil respiration from snow-scoured alpine tundra, *J. Geophys. Res. G Biogeosciences*, 121(4), 1118–1130,
737 doi:10.1002/2015JG003081, 2016.
- 738 Kratzert, F., Klotz, D., Brenner, C., Schulz, K. and Herrnegger, M.: Rainfall–runoff modelling using Long Short-Term
739 Memory (LSTM) networks, *Hydrol. Earth Syst. Sci.*, 22(11), 6005–6022, doi:10.5194/hess-22-6005-2018, 2018.
- 740 Lasslop, G., Reichstein, M., Papale, D., Richardson, A., Arneeth, A., Barr, A., Stoy, P. and Wohlfahrt, G.: Separation
741 of net ecosystem exchange into assimilation and respiration using a light response curve approach: Critical issues and
742 global evaluation, *Glob. Chang. Biol.*, 16(1), 187–208, doi:10.1111/j.1365-2486.2009.02041.x, 2010.
- 743 Livingston, G. P. and Hutchinson, G. L.: Enclosure-based measurement of trace gas exchange: applications and
744 sources of error., 1995.
- 745 Ma, Y., Liu, S., Song, L., Xu, Z., Liu, Y., Xu, T. and Zhu, Z.: Estimation of daily evapotranspiration and irrigation
746 water efficiency at a Landsat-like scale for an arid irrigation area using multi-source remote sensing data, *Remote
747 Sens. Environ.*, 216(August), 715–734, doi:10.1016/j.rse.2018.07.019, 2018.
- 748 McCabe, M. F., Aragon, B., Houborg, R. and Mascaro, J.: CubeSats in Hydrology: Ultrahigh-Resolution Insights Into
749 Vegetation Dynamics and Terrestrial Evaporation, *Water Resour. Res.*, 53(12), 10017–10024,
750 doi:10.1002/2017WR022240, 2017.
- 751 Metzger, S., Junkermann, W., Mauder, M., Butterbach-Bahl, K., Trancón Y Widemann, B., Neidl, F., Schäfer, K.,
752 Wieneke, S., Zheng, X. H., Schmid, H. P. and Foken, T.: Spatially explicit regionalization of airborne flux
753 measurements using environmental response functions, *Biogeosciences*, 10(4), 2193–2217, doi:10.5194/bg-10-2193-
754 2013, 2013.
- 755 Migliavacca, M., Reichstein, M., Richardson, A. D., Mahecha, M. D., Cremonese, E., Delpierre, N., Galvagno, M.,
756 Law, B. E., Wohlfahrt, G., Andrew Black, T., Carvalhais, N., Ceccherini, G., Chen, J., Gobron, N., Koffi, E., William
757 Munger, J., Perez-Priego, O., Robustelli, M., Tomelleri, E. and Cescatti, A.: Influence of physiological phenology on
758 the seasonal pattern of ecosystem respiration in deciduous forests, *Glob. Chang. Biol.*, 21(1), 363–376,
759 doi:10.1111/gcb.12671, 2015.
- 760 Mohanty, B. P., Cosh, M. H., Lakshmi, V. and Montzka, C.: Soil moisture remote sensing: State-of-the-science,
761 *Vadose Zo. J.*, doi:10.2136/vzj2016.10.0105, 2017.
- 762 Mu, Q., Zhao, M. and Running, S. W.: MODIS Global Terrestrial Evapotranspiration (ET) Product (MOD16A2/A3),
763 *Algorithm Theor. Basis Doc.*, 2013.
- 764 NASA: Moderate Resolution Imaging Spectroradiometer (MODIS) Overview, Nasa, 2008.
- 765 Ng, G., Bedford, D. and Miller, D.: A mechanistic modeling and data assimilation framework for Mojave Desert
766 ecohydrology, *Water Resour. Res.*, 4662–4685, doi:10.1002/2014WR015281.Received, 2014.
- 767 Olah, C.: Understanding LSTM Networks, <https://colah.github.io/posts/2015-08-Understanding-LSTMs/>, 2015, 2015.
- 768 Oleson, K. W., Lawrence, D. M., Bonan, G. B., Drevniak, B., Huang, M., Koven, C. D., Levis, S., Li, F., Riley, J.,
769 Subin, Z. M., Swenson, S. C., Thornton, P. E., Bozbiyik, A., Fisher, R. A., Heald, C. L., Kluzek, E., Lamarque, J.-F.,
770 Lawrence, P. J., Leung, L. R., Lipscomb, W., Muszala, S., Ricciuto, D. M., Sacks, W. J., Sun, Y., Tang, J. and Yang,



- 771 Z.-L.: Technical Description of version 4.5 of the Community Land Model (CLM)., 2013.
- 772 Omernik, J. M.: Perspectives on the nature and definition of ecological regions., *Environ. Manage.*,
773 doi:10.1007/s00267-003-5197-2, 2004.
- 774 Omernik, J. M. and Griffith, G. E.: Ecoregions of the Conterminous United States: Evolution of a Hierarchical Spatial
775 Framework, *Environ. Manage.*, doi:10.1007/s00267-014-0364-1, 2014.
- 776 Oyler, J. W., Dobrowski, S. Z., Ballantyne, A. P., Klene, A. E. and Running, S. W.: Artificial amplification of warming
777 trends across the mountains of the western United States, *Geophys. Res. Lett.*, doi:10.1002/2014GL062803, 2015.
- 778 Paca, V. H. da M., Espinoza-Dávalos, G. E., Hessels, T. M., Moreira, D. M., Comair, G. F. and Bastiaanssen, W. G.
779 M.: The spatial variability of actual evapotranspiration across the Amazon River Basin based on remote sensing
780 products validated with flux towers, *Ecol. Process.*, 8(1), doi:10.1186/s13717-019-0158-8, 2019.
- 781 Pelletier, J. D., Barron-Gafford, G. A., Gutiérrez-Jurado, H., Hinckley, E. L. S., Istanbuloglu, E., McGuire, L. A.,
782 Niu, G. Y., Poulos, M. J., Rasmussen, C., Richardson, P., Swetnam, T. L. and Tucker, G. E.: Which way do you lean?
783 Using slope aspect variations to understand Critical Zone processes and feedbacks, *Earth Surf. Process. Landforms*,
784 doi:10.1002/esp.4306, 2018.
- 785 PRIESTLEY, C. H. B. and TAYLOR, R. J.: On the Assessment of Surface Heat Flux and Evaporation Using Large-
786 Scale Parameters, *Mon. Weather Rev.*, doi:10.1175/1520-0493(1972)100<0081:otaosh>2.3.co;2, 1972.
- 787 Pumpanen, J., Kolari, P., Ilvesniemi, H., Minkkinen, K., Vesala, T., Niinistö, S., Lohila, A., Larmola, T., Morero, M.,
788 Pihlatie, M., Janssens, I., Yuste, J. C., Grünzweig, J. M., Reth, S., Subke, J. A., Savage, K., Kutsch, W., Østreg, G.,
789 Ziegler, W., Anthoni, P., Lindroth, A. and Hari, P.: Comparison of different chamber techniques for measuring soil
790 CO₂ efflux, *Agric. For. Meteorol.*, doi:10.1016/j.agrformet.2003.12.001, 2004.
- 791 Qiao, Z., Xu, X., Zhao, M., Wang, F. and Liu, L.: The application of a binary division procedure to the classification
792 of forest subcategories using MODIS time-series data during 2000–2010 in China, *Int. J. Remote Sens.*,
793 doi:10.1080/01431161.2016.1176269, 2016.
- 794 Reichstein, M., Falge, E., Baldocchi, D., Papale, D., Aubinet, M., Berbigier, P., Bernhofer, C., Buchmann, N.,
795 Gilmanov, T., Granier, A., Grünwald, T., Havránková, K., Ilvesniemi, H., Janous, D., Knohl, A., Laurila, T., Lohila,
796 A., Loustau, D., Matteucci, G., Meyers, T., Miglietta, F., Ourcival, J. M., Pumpanen, J., Rambal, S., Rotenberg, E.,
797 Sanz, M., Tenhunen, J., Seufert, G., Vaccari, F., Vesala, T., Yakir, D. and Valentini, R.: On the separation of net
798 ecosystem exchange into assimilation and ecosystem respiration: Review and improved algorithm, *Glob. Chang. Biol.*,
799 doi:10.1111/j.1365-2486.2005.001002.x, 2005.
- 800 Reichstein, M., Camps-Valls, G., Stevens, B., Jung, M., Denzler, J., Carvalhais, N. and Prabhat: Deep learning and
801 process understanding for data-driven Earth system science, *Nature*, 566(7743), 195–204, doi:10.1038/s41586-019-
802 0912-1, 2019.
- 803 Ren, H., Cromwell, E., Kravitz, B. and Chen, X.: Using Deep Learning to Fill Spatio-Temporal Data Gaps in
804 Hydrological Monitoring Networks, *Hydrol. Earth Syst. Sci. Discuss.*, (May), 1–20, doi:10.5194/hess-2019-196, 2019.
- 805 Rungee, J., Bales, R. and Goulden, M.: Evapotranspiration response to multiyear dry periods in the semiarid western
806 United States, *Hydrol. Process.*, doi:10.1002/hyp.13322, 2019.
- 807 Ryu, Y., Baldocchi, D. D., Kobayashi, H., Van Ingen, C., Li, J., Black, T. A., Beringer, J., Van Gorsel, E., Knohl, A.,
808 Law, B. E. and Rouspard, O.: Integration of MODIS land and atmosphere products with a coupled-process model to
809 estimate gross primary productivity and evapotranspiration from 1 km to global scales, *Global Biogeochem. Cycles*,
810 25(4), 1–24, doi:10.1029/2011GB004053, 2011.
- 811 Schimel, D., Kittel, T. G. F., Running, S., Monson, R., Turnipseed, A. and Anderson, D.: Carbon sequestration studied
812 in Western U.S. mountains, *Eos (Washington, DC)*, doi:10.1029/2002EO000314, 2002.
- 813 Seneviratne, S. I., Lüthi, D., Litschi, M. and Schär, C.: Land-atmosphere coupling and climate change in Europe,
814 *Nature*, doi:10.1038/nature05095, 2006.
- 815 Speckman, H. N., Frank, J. M., Bradford, J. B., Miles, B. L., Massman, W. J., Parton, W. J. and Ryan, M. G.: Forest



- 816 ecosystem respiration estimated from eddy covariance and chamber measurements under high turbulence and
817 substantial tree mortality from bark beetles, *Glob. Chang. Biol.*, doi:10.1111/gcb.12731, 2015.
- 818 Strachan, S., Kelsey, E. P., Brown, R. F., Dascalu, S., Harris, F., Kent, G., Lyles, B., McCurdy, G., Slater, D. and
819 Smith, K.: Filling the Data Gaps in Mountain Climate Observatories Through Advanced Technology, Refined
820 Instrument Siting, and a Focus on Gradients, *Mt. Res. Dev.*, 36(4), 518–527, doi:10.1659/mrd-journal-d-16-00028.1,
821 2016.
- 822 Suleau, M., Moureaux, C., Dufranne, D., Buysse, P., Bodson, B., Destain, J. P., Heinesch, B., Debacq, A. and Aubinet,
823 M.: Respiration of three Belgian crops: Partitioning of total ecosystem respiration in its heterotrophic, above- and
824 below-ground autotrophic components, *Agric. For. Meteorol.*, doi:10.1016/j.agrformet.2011.01.012, 2011.
- 825 Teuling, A. J., Van Loon, A. F., Seneviratne, S. I., Lehner, I., Aubinet, M., Heinesch, B., Bernhofer, C., Grünwald,
826 T., Prasse, H. and Spank, U.: Evapotranspiration amplifies European summer drought, *Geophys. Res. Lett.*,
827 doi:10.1002/grl.50495, 2013.
- 828 Thornton, P. E., Thornton, M. M., Mayer, B. W., Wei, Y., Devarakonda, R., Vose, R. S. and Cook, R. B.: Daymet:
829 Daily Surface Weather Data on a 1-km Grid for North America, Version 3, ORNL DAAC, Oak Ridge, Tennessee,
830 USA, 2017.
- 831 Tran, A. P., Rungee, J., Faybishenko, B., Dafflon, B. and Hubbard, S. S.: Assessment of spatiotemporal variability of
832 evapotranspiration and its governing factors in a mountainous watershed, *Water (Switzerland)*, 11(2),
833 doi:10.3390/w11020243, 2019.
- 834 U.S. Environmental Protection Agency: Level III Ecoregions of the Continental United States, *Environ. Prot.*, 2003.
- 835 Viviroli, D. and Weingartner, R.: “Water towers”—A global view of the hydrological importance of mountains, in
836 *Advances in Global Change Research.*, 2008.
- 837 Viviroli, D., Dürr, H. H., Messerli, B., Meybeck, M. and Weingartner, R.: Mountains of the world, water towers for
838 humanity: Typology, mapping, and global significance, *Water Resour. Res.*, 43(7), 1–13,
839 doi:10.1029/2006WR005653, 2007.
- 840 Vogelmann, J. E., Howard, S. M., Yang, L., Larson, C. R., Wylie, B. K. and Van Driel, N.: Completion of the 1990s
841 National Land Cover Data set for the conterminous United States from Landsat thematic mapper data and ancillary
842 data sources, *Photogramm. Eng. Remote Sensing*, 2001.
- 843 Wang, B., Zha, T. S., Jia, X., Wu, B., Zhang, Y. Q. and Qin, S. G.: Soil moisture modifies the response of soil
844 respiration to temperature in a desert shrub ecosystem, *Biogeosciences*, 11(2), 259–268, doi:10.5194/bg-11-259-2014,
845 2014.
- 846 Webb, R. W., Fassnacht, S. R. and Gooseff, M. N.: Hydrologic flow path development varies by aspect during spring
847 snowmelt in complex subalpine terrain, *Cryosphere*, 12(1), 287–300, doi:10.5194/tc-12-287-2018, 2018.
- 848 Williams, C. A. and Albertson, J. D.: Soil moisture controls on canopy-scale water and carbon fluxes in an African
849 savanna, *Water Resour. Res.*, doi:10.1029/2004WR003208, 2004.
- 850 Williams, M., Richardson, A. D., Reichstein, M., Stoy, P. C., Peylin, P., Verbeeck, H., Carvalhais, N., Jung, M.,
851 Hollinger, D. Y., Kattge, J., Leuning, R., Luo, Y., Tomelleri, E., Trudinger, C. and Wang, Y.-P.: Improving land
852 surface models with FLUXNET data, *Biogeosciences Discuss.*, doi:10.5194/bgd-6-2785-2009, 2009.
- 853 Wilson, K. B., Hanson, P. J., Mulholland, P. J., Baldocchi, D. D. and Wullschlegel, S. D.: A comparison of methods
854 for determining forest evapotranspiration and its components: Sap-flow, soil water budget, eddy covariance and
855 catchment water balance, *Agric. For. Meteorol.*, 106(2), 153–168, doi:10.1016/S0168-1923(00)00199-4, 2001.
- 856 Xiao, J., Ollinger, S. V., Frolking, S., Hurtt, G. C., Hollinger, D. Y., Davis, K. J., Pan, Y., Zhang, X., Deng, F., Chen,
857 J., Baldocchi, D. D., Law, B. E., Arain, M. A., Desai, A. R., Richardson, A. D., Sun, G., Amiro, B., Margolis, H., Gu,
858 L., Scott, R. L., Blanken, P. D. and Suyker, A. E.: Data-driven diagnostics of terrestrial carbon dynamics over North
859 America, *Agric. For. Meteorol.*, doi:10.1016/j.agrformet.2014.06.013, 2014.
- 860 Xu, L., Baldocchi, D. D. and Tang, J.: How soil moisture, rain pulses, and growth alter the response of ecosystem



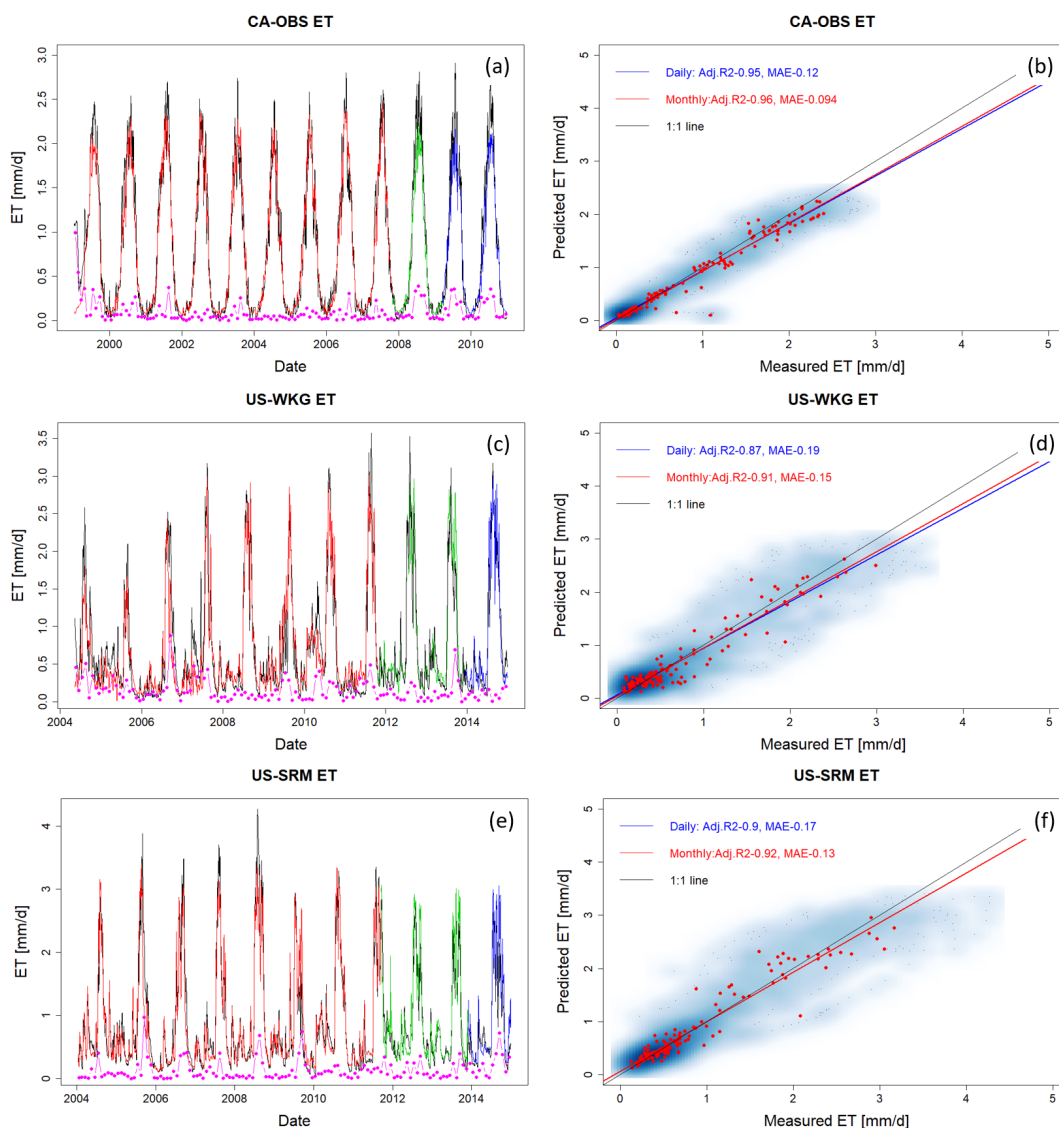
- 861 respiration to temperature, *Global Biogeochem. Cycles*, 18(4), 1–10, doi:10.1029/2004GB002281, 2004.
- 862 Xu, T., Guo, Z., Liu, S., He, X., Meng, Y., Xu, Z., Xia, Y., Xiao, J., Zhang, Y., Ma, Y. and Song, L.: Evaluating
863 Different Machine Learning Methods for Upscaling Evapotranspiration from Flux Towers to the Regional Scale, *J.*
864 *Geophys. Res. Atmos.*, 123(16), 8674–8690, doi:10.1029/2018JD028447, 2018.
- 865 Zhang, L., Potter, N., Hickel, K., Zhang, Y. and Shao, Q.: Water balance modeling over variable time scales based on
866 the Budyko framework - Model development and testing, *J. Hydrol.*, 360(1–4), 117–131,
867 doi:10.1016/j.jhydrol.2008.07.021, 2008.
- 868 Zhang, Y., Kong, D., Gan, R., Chiew, F. H. S., McVicar, T. R., Zhang, Q. and Yang, Y.: Coupled estimation of 500 m
869 and 8-day resolution global evapotranspiration and gross primary production in 2002–2017, *Remote Sens. Environ.*,
870 222(May 2018), 165–182, doi:10.1016/j.rse.2018.12.031, 2019.

871

872 **Appendix**

873

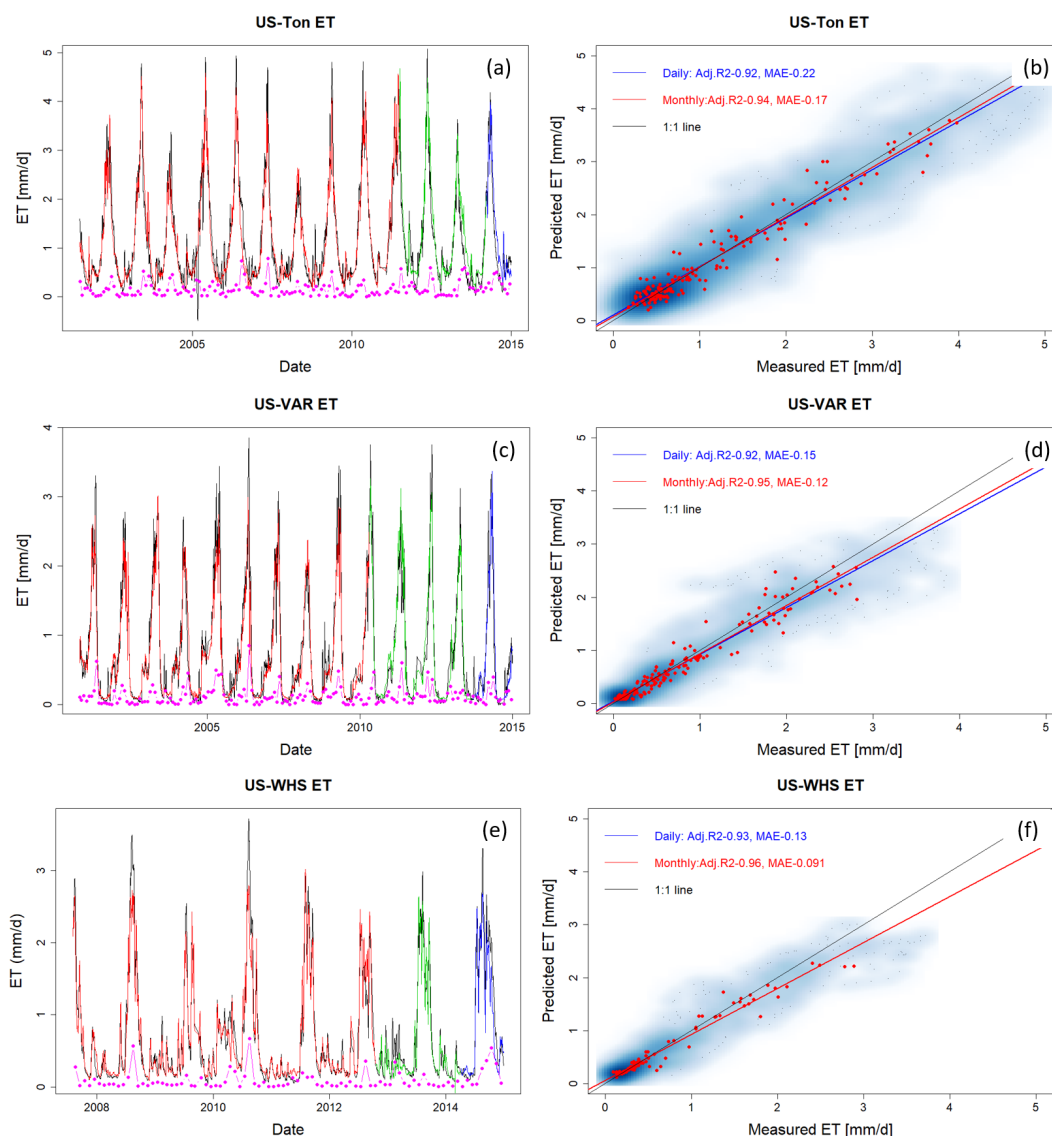
874 **1. ET and R_{ECO} Estimation over Time at other Fluxnet sites**



875

876 **Figure A1: ET estimation with data from selected FLUXNET sites at CA-OBS, US-Wkg, and US-SRM. Panels (a), (c), and**
877 **(e) present daily estimations of ET with red, green, and blue lines representing data used for training, validation, and**
878 **prediction, respectively, and the black line representing the eddy covariance measurement. Pink points describe monthly**
879 **mean difference between HPM estimation and measured data. Panels (b), (d), and (f) show the scatter plots of daily (blue)**
880 **and monthly (red) ET. Darker blue clouds represent greater density of data points.**

881

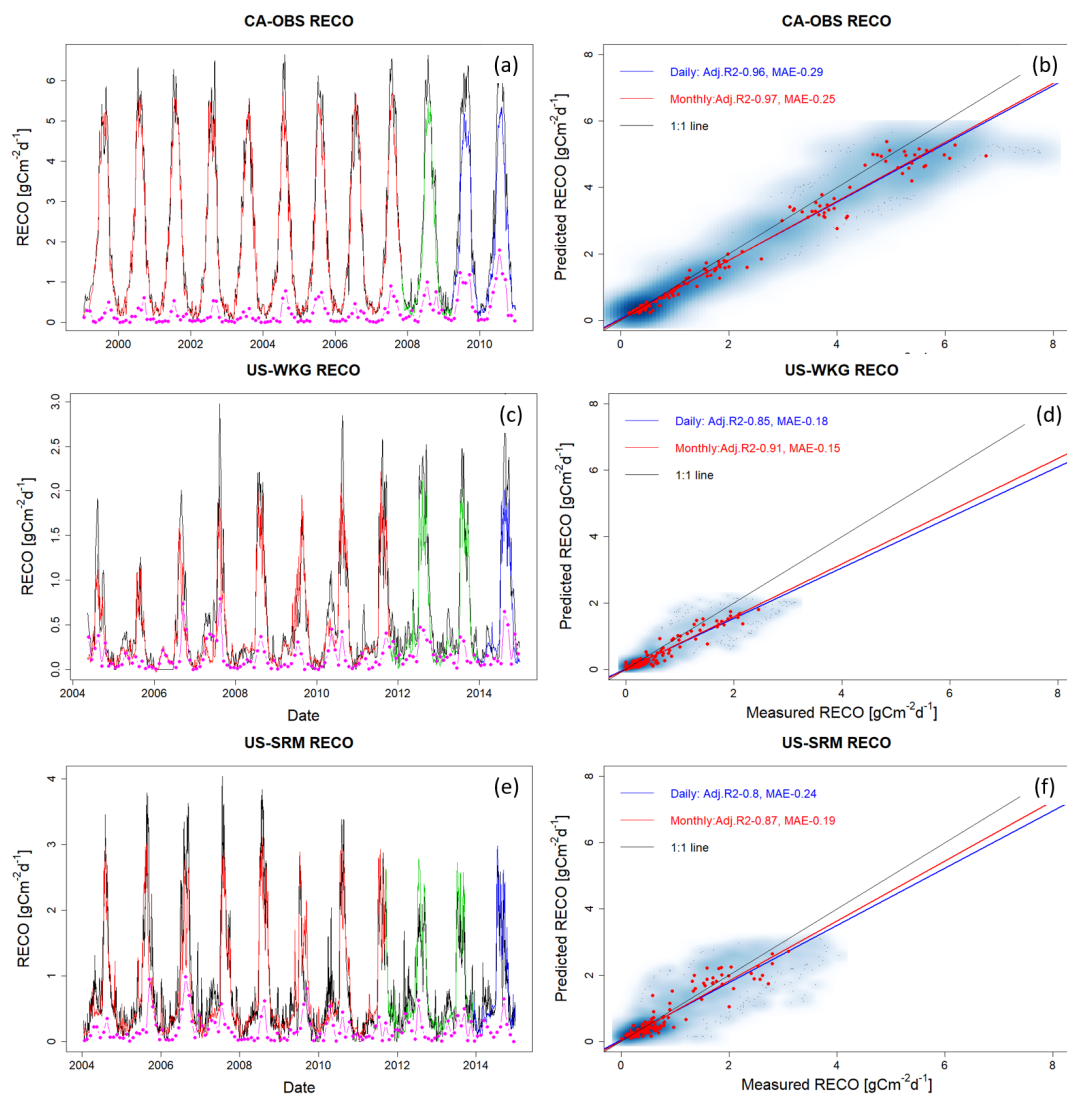


882

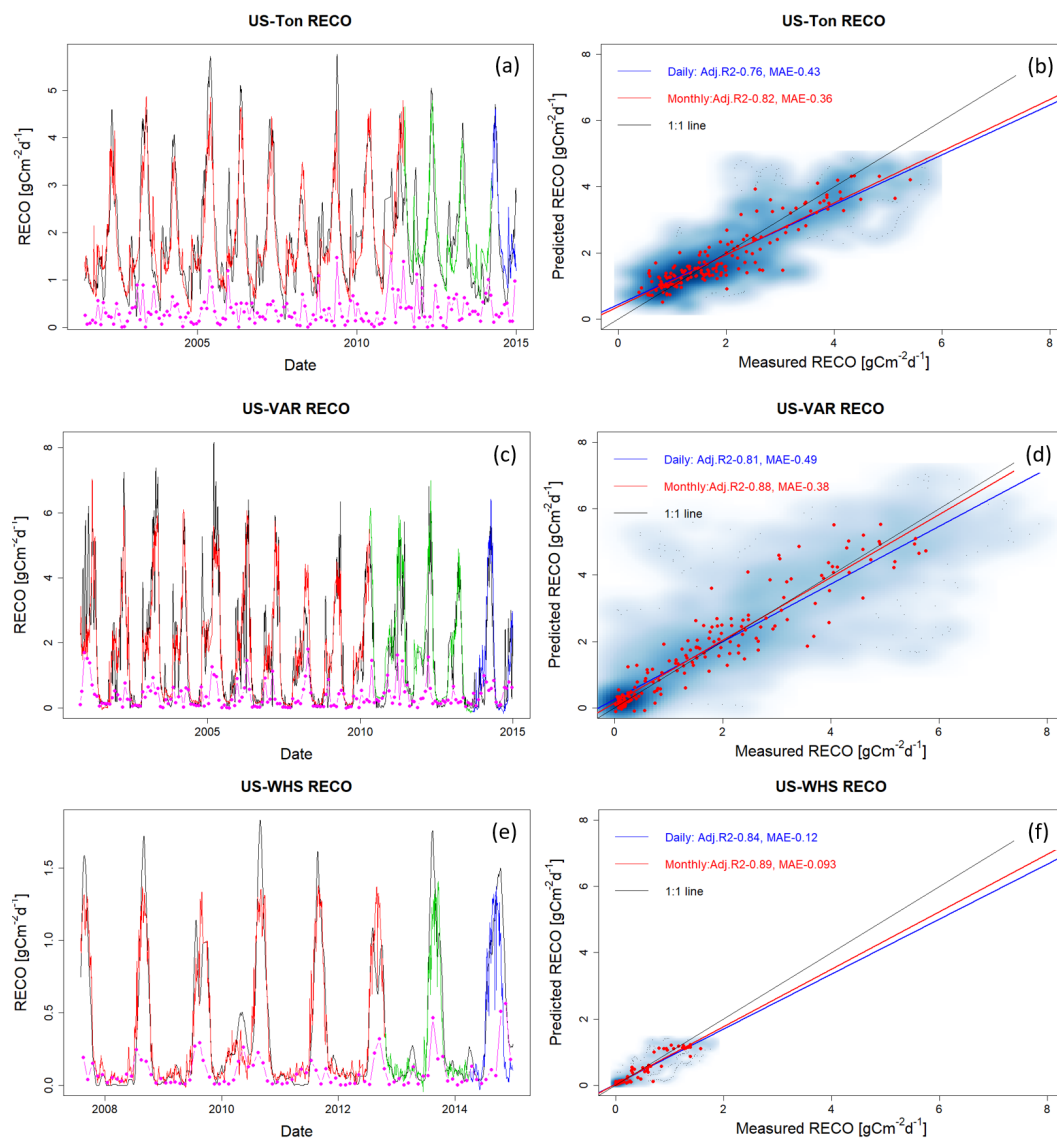
883 **Figure A2: ET estimation with data from selected FLUXNET sites at US-Ton, US-Var, and US-Whs. Panels (a), (c), and**
884 **(e) present daily estimations of ET with red, green, and blue lines representing data used for training, validation, and**
885 **prediction, respectively, and the black line representing the eddy covariance measurement. Pink points describe monthly**
886 **mean difference between HPM estimation and measured data. Panels (b), (d), and (f) show the scatter plots of daily (blue)**
887 **and monthly (red) ET. Darker blue clouds represent greater density of data points.**

888

889



890
891 **Figure A3:** R_{ECO} estimation with data from selected FLUXNET sites at CA-OBS, US-Wkg, and US-SRM. Panels (a), (c),
892 and (e) present daily estimations of R_{ECO} with red, green, and blue lines representing data used for training, validation, and
893 prediction, respectively, and the black line is eddy covariance measurement. Pink points describe the monthly mean
894 difference between HPM estimation and measured data. Panels (b), (d), and (f) show the scatter plots of daily (blue) and
895 monthly (red) R_{ECO} . Darker blue clouds represent greater density of data points.
896



897

898 **Figure A4:** R_{ECO} estimation with data from selected FLUXNET sites at US-Ton, US-Var, and US-Whs. Panels (a), (c), and
 899 (e) present daily estimations of R_{ECO} with red, green, and blue lines representing data used for training, validation, and
 900 prediction, respectively, and the black line representing the eddy covariance measurement. Pink points describe monthly
 901 mean difference between HPM estimation and measured data. Panels (b), (d), and (f) show the scatter plots of daily (blue)
 902 and monthly (red) R_{ECO} . Darker blue clouds represent greater density of data points.

903

904